



Publication Year	2019
Acceptance in OA@INAF	2020-12-21T16:24:10Z
Title	A Simplified, Lossless Reanalysis of PAPER-64
Authors	Kolopanis, Matthew; Jacobs, Daniel C.; Cheng, Carina; Parsons, Aaron R.; Kohn, Saul A.; et al.
DOI	10.3847/1538-4357/ab3e3a
Handle	http://hdl.handle.net/20.500.12386/29067
Journal	THE ASTROPHYSICAL JOURNAL
Number	883



A Simplified, Lossless Reanalysis of PAPER-64

Matthew Kolopanis¹, Daniel C. Jacobs¹, Carina Cheng², Aaron R. Parsons^{2,3}, Saul A. Kohn⁴, Jonathan C. Pober⁵, James E. Aguirre⁴, Zaki S. Ali², Gianni Bernardi^{6,7,8}, Richard F. Bradley^{9,10,11}, Chris L. Carilli^{12,13}, David R. DeBoer³, Matthew R. Dexter³, Joshua S. Dillon^{2,16}, Joshua Kerrigan⁵, Pat Klima¹⁰, Adrian Liu^{14,15}, David H. E. MacMahon³, David F. Moore⁴, Nithyanandan Thyagarajan^{12,17}, Chuneeta D. Nunhokee⁷, William P. Walbrugh⁶, and Andre Walker⁶

¹School of Earth and Space Exploration, Arizona State University, Tempe AZ, USA; matthew.kolopanis@asu.edu

²Astronomy Department, University of California, Berkeley, CA, USA

³Radio Astronomy Laboratory, University of California, Berkeley CA, USA

⁴Department of Physics and Astronomy, University of Pennsylvania, Philadelphia PA, USA

⁵Department of Physics, Brown University, Providence RI, USA

⁶INAF-Istituto di Radioastronomia, via Gobetti 101, I-40129, Bologna, Italy

⁷Department of Physics and Electronics, Rhodes University, PO Box 94, Grahamstown, 6140, South Africa

⁸South African Radio Astronomy Observatory, Black River Park, 2 Fir Street, Observatory, Cape Town, 7925, South Africa

⁹Department of Electrical and Computer Engineering, University of Virginia, Charlottesville VA, USA

¹⁰National Radio Astronomy Observatory, Charlottesville VA, USA

¹¹Department of Astronomy, University of Virginia, Charlottesville VA, USA

¹²National Radio Astronomy Observatory, Socorro, NM, USA

¹³Cavendish Laboratory, Cambridge, UK

¹⁴Department of Physics and McGill Space Institute, McGill University, Montreal, QC, Canada

¹⁵CIFAR Azrieli Global Scholar, Gravity & the Extreme Universe Program, Canadian Institute for Advanced Research, 661 University Avenue, Suite 505, Toronto, Ontario M5G 1M1, Canada

Received 2019 May 3; revised 2019 July 25; accepted 2019 August 23; published 2019 September 27

Abstract

We present limits on the 21 cm power spectrum from the Epoch of Reionization using data from the 64 antenna configuration of the Donald C. Backer Precision Array for Probing the Epoch of Reionization (PAPER) analyzed through a power spectrum pipeline independent from previous PAPER analyses. Previously reported results from PAPER have been found to contain significant signal loss. Several lossy steps from previous PAPER pipelines have not been included in this analysis, namely delay-based foreground filtering, optimal fringe-rate filtering, and empirical covariance-based estimators. Steps that remain in common with previous analyses include redundant calibration and local sidereal time (LST) binning. The power spectra reported here are effectively the result of applying a linear Fourier transform analysis to the calibrated, LST-binned data. This analysis also uses more data than previous publications, including the complete available redshift range of $z \sim 7.5$ to 11. In previous PAPER analyses, many power spectrum measurements were found to be detections of noncosmological power at levels of significance ranging from two to hundreds of times the theoretical noise. Here, excess power is examined using redundancy between baselines and power spectrum jackknives. The upper limits we find on the 21 cm power spectrum from reionization are $(1500 \text{ mK})^2$, $(1900 \text{ mK})^2$, $(280 \text{ mK})^2$, $(200 \text{ mK})^2$, $(380 \text{ mK})^2$, and $(300 \text{ mK})^2$ at redshifts $z = 10.87$, 9.93, 8.68, 8.37, 8.13, and 7.48, respectively. For reasons described in Cheng et al., these limits supersede all previous PAPER results.

Key words: dark ages, reionization, first stars

1. Introduction

The Epoch of Reionization (EoR) represents a global phase transition for intergalactic hydrogen from a neutral to ionized state. In most models, this phase transition is fueled by the first luminous bodies, which condensed from hydrogen clouds and began heating and ionizing the surrounding intergalactic medium (IGM; Barkana & Loeb 2001; Oh 2001). Observational constraints limit the timing of this event to somewhere in the redshift range ($12 < z < 6$).

The 21 cm photons emitted from the spin-flip transition of hydrogen are predicted to be a powerful probe of cosmic evolution during this time (Furlanetto et al. 2006). For in-depth reviews of the physics of 21 cm cosmology, refer to Barkana & Loeb (2007), Morales & Wyithe (2010), Loeb & Furlanetto (2013), and Pritchard & Loeb (2010).

As observed from Earth, the 21 cm line is redshifted into the 100 MHz radio band, where it competes with human interference and astrophysical emission from both the Milky Way and other galaxies. Interference is mitigated by careful radio frequency (RF) design and choosing a remote and regulated location for observation,¹⁸ leaving astrophysical foregrounds as the principal contaminant, dominating the cosmological 21 cm background by four or five orders of magnitude. The foreground challenges faced by modern radio arrays have been discussed in detail in previous literature (e.g., Santos et al. 2005; Ali et al. 2008; de Oliveira-Costa et al. 2008; Bernardi et al. 2009, 2010, 2013; Ghosh et al. 2011; Pober et al. 2013; Yatawatta et al. 2013).

Detection of 21 cm emission by the neutral hydrogen medium is the target of multiple experiments including those aimed at a globally averaged total power measurement

¹⁶ NSF AAPF Fellow.

¹⁷ Jansky Fellow of the National Radio Astronomy Observatory.

¹⁸ PAPER was located at the South Africa Square Kilometer Array close to the current home of Meerkat.

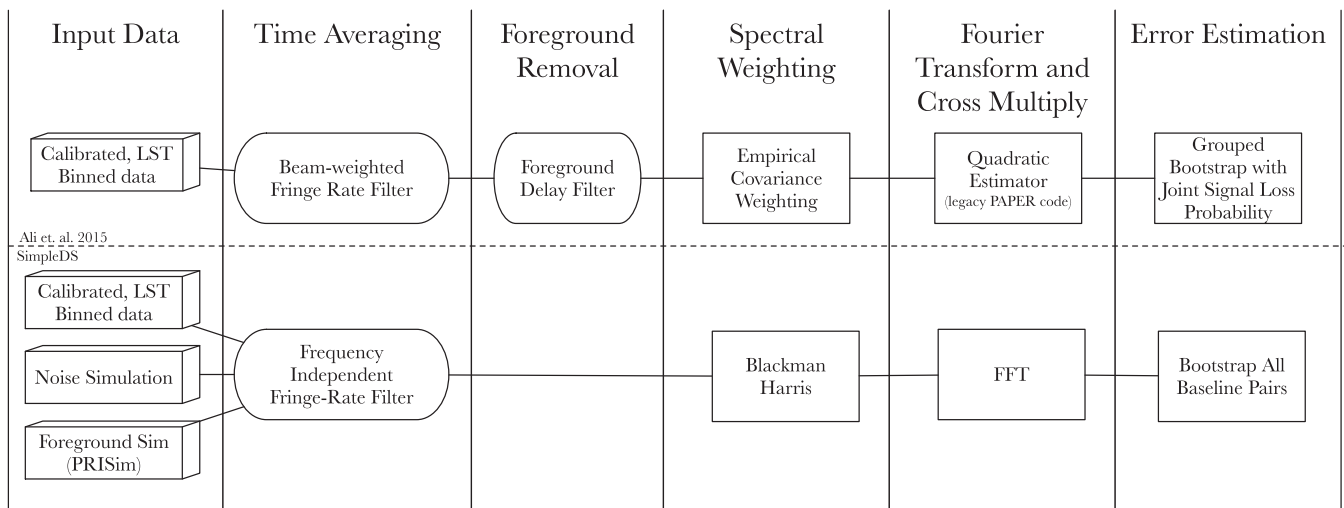


Figure 1. Comparison between the prior PAPER analysis by Ali et al. (2015) and “simpleDS.” The frequency-independent fringe-rate filter has a smoother delay response compared to the one used in A15 and C18 in order to reduce leakage of foreground power outside the wedge. The delay filter for foreground removal has been omitted from this analysis to keep the pipeline as simple as possible. While the foreground removal technique should not affect cosmological signals outside the wedge (Parsons & Backer 2009; Parsons et al. 2012b, 2014), recent works have shown that the use of this filter does not produce a statistically significant reduction in power at high-delay modes (Kerrigan et al. 2018). Also, we find that the Fourier transform from frequency into delay is not dynamic range limited when including the foreground signals. Most importantly, in order to avoid signal loss during power spectrum estimation, we use a uniformly weighted fast Fourier transform (FFT) estimator instead of the empirical inverse covariance weighted OQE used in previous PAPER works.

(EDGES, Bowman & Rogers 2010; LEDA, Bernardi et al. 2016; SARAS, Patra et al. 2015; BIGHORNS, Sokolowski et al. 2015; SCI-HI, Voytek et al. 2014) and the fluctuations caused by heating, cooling, collapse, and ionization (GMRT, Paciga et al. 2013; LOFAR,¹⁹ Yatawatta et al. 2013; MWA,²⁰ Tingay et al. 2013; HERA,²¹ DeBoer et al. 2017).

The Donald C. Backer Precision Array for Probing the Epoch of Reionization (PAPER²²; Parsons et al. 2010) was an experimental interferometer with the goal of placing some of the first limits on these fluctuations. The PAPER experiment observed in stages, with the number of antennas increasing by factors of 2 roughly every year. Previous PAPER publications include the eight-station results (Parsons et al. 2010), the 32 element power spectrum estimates (Poher et al. 2013; Parsons et al. 2014; Jacobs et al. 2015; Moore et al. 2017), the 64 element power spectrum estimates (Ali et al. 2015; hereafter A15), and our companion paper (Cheng et al. 2018, hereafter C18).

Through the reanalysis described in C18, additional signal loss in the empirical covariance inversion method was discovered (Ali et al. 2018). Signal loss is the unintentional removal of the target cosmological signal during analysis. In A15, this results from the use of empirically estimated covariance matrices as a weighting matrix in the quadratic estimator (QE) during power spectrum estimation. An empirically estimated covariance matrix contains terms related to the data; this dependence induces higher order (i.e., non-quadratic) terms in the estimator. Applying QE normalization despite these terms then violates the assumptions of the statistics of the QEs and produces a biased result with incorrect power levels (e.g., signal loss). This effect is described more thoroughly in Section 3.1.1 of C18. C18 also describes how the amount of signal loss in the A15 analysis was underestimated and was further obfuscated by similarly underestimated uncertainties (from both

analytic noise estimates and bootstrapped error bars). The C18 analysis presents a detailed look at the origin of these issues but does not deliver a revised analysis for the same data. In this paper, we take a different look using an independently developed pipeline, which conservatively has had many lossy steps removed (see Figure 1).

Specifically, we aim to make improvements in two areas. First, we use the independently developed pipeline SIMPLEDS,²³ which has minimal common code with the original PAPER pipeline built for A15 and extended by C18. Second, this analysis reduces the number of pipeline steps. The basic concept of the delay spectrum is retained with a power spectrum measurement coming from each type of baseline; however several steps have been removed and others replaced. The steps used in this type of analysis can be broken into three sections: calibration and averaging over multiple nights (LST binning), foreground filtering and time averaging, and power spectrum estimation.

The reanalysis described in C18 focused almost exclusively on the final stage. In this analysis, the intermediate stages (like foreground filtering) have been re-examined, and in all cases either removed or simplified. This paper uses data sets that have been previously interference flagged, calibrated with redundant calibration, LST binned, and absolutely calibrated to Pictor A. As this analysis takes advantage of archival LST-binned data products, the stages prior to binning are unchanged from previous analyses.

This paper is organized as follows: we discuss the three pipeline inputs by reviewing the data used in this analysis in Section 2, the input noise simulation in Section 3, and the simulated sky input used to calibrate power spectrum normalization and examine additional signal loss in Section 4. The major changes in the analysis pipelines between this work and A15 are discussed in Section 5. We investigate how closely the PAPER baselines adhere to the redundant layout in Section 6. In Section 7, we review the revised power spectrum estimation techniques and uncertainties. The multiredshift

¹⁹ www.lofar.org

²⁰ mwatelescope.org

²¹ reionization.org

²² cor.berkeley.edu

²³ github.com/RadioAstronomySoftwareGroup/simpleDS

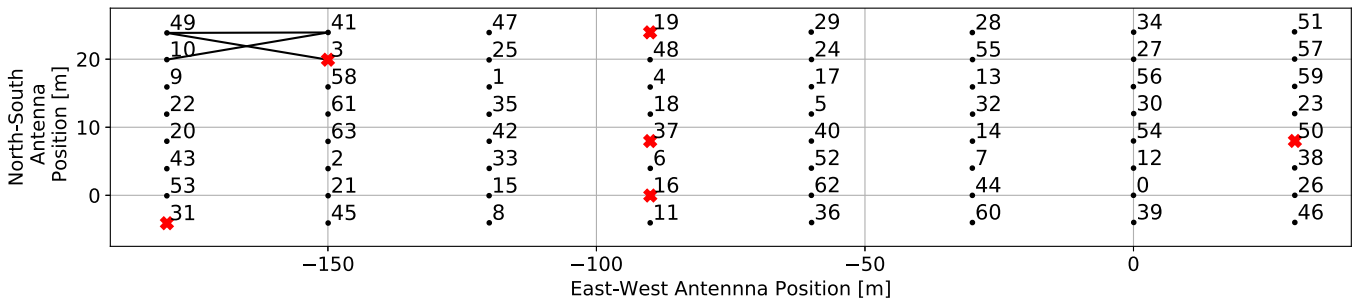


Figure 2. The antenna positions of PAPER-64. Highlighted are the three baseline types used in this analysis. These baselines consist of east–west baselines from adjacent antenna columns with no row separation (e.g., 49–41, 1–4, 0–26), baselines with one column separation and one positive northward row separation (e.g., 10–41, 1–48, 0–38), and baselines with one column separation and one negative northward row separation (e.g., 49–3, 1–18, 0–46). A red “x” denotes antennas that have been flagged from analysis. Reasons for flagging include previously known spectral instability (19, 37, and 50), low number of counts in LST binning (3 and 16), and suspected nonredundant information (31).

power spectrum results are presented in Section 8, and upper limits on the 21 cm power spectrum are presented in Section 9. Finally, we provide some concluding remarks in Section 10.

2. Data

In the next three sections, we discuss the three major inputs to our power spectrum pipeline: the observed data, simulated thermal noise, and the simulated foreground visibilities in Sections 2–4, respectively.

2.1. Data Selection

The PAPER-64 antennas were arranged in an 8×8 grid as illustrated in Figure 2. The grid arrangement enables many repeated measurements of a single spatial Fourier mode to be averaged together before squaring, which delivers higher sensitivity for these PAPER elements than a nonredundant configuration (Parsons et al. 2012a). This configuration is also well matched to the delay spectrum method of measuring the power spectrum where visibilities are Fourier-transformed along the spectral dimension to make a one-dimensional slice through the three-dimensional Fourier domain (Parsons et al. 2012b).

In principle, the delay spectrum method can be used to approximate a power spectrum for every pair of antennas, which allows a great deal of freedom to explore systematic effects that vary from antenna pair to antenna pair. However, in this analysis, we limit our data volume by only forming power spectra from select baselines. Specifically, we use only three baseline types of the shortest length (30 m) as illustrated in Figure 2. The shortest baselines are the most numerous and therefore provide the most sensitive measurements. The shortest baselines also probe what are likely to be the brightest modes of the diffuse reionization power spectrum. However, the shortest spacings are also sensitive to diffuse foreground power, which is known to be brighter than the extragalactic point source background on these scales (Beardsley et al. 2016). The exact tradeoffs between foregrounds, calibration error, and sensitivity are a matter of ongoing research.

The data used here come from the PAPER-64 season which ran for 135 nights between 2012 November 8 (JD 2456240) and 2013 March 23 (JD 24563745). Three antennas (19, 37, and 50) have been flagged due to higher levels of spectral instability and were also flagged in A15.

2.2. Calibration and LST Binning

The analysis described here begins with data that were previously compressed, calibrated, and LST binned. The details of the compression, calibration, and binning process are described more completely in A15; here, we briefly describe the salient details. Compression is achieved with the application of a fringe-rate filter (FRF; described in more detail in Section 5.1) and a wideband iterative deconvolution algorithm (WIDA; described in more detail in Section 5.2) to limit the data to fringe rates less than $f \lesssim 23$ mHz and delays less than $|\tau| \lesssim 1 \mu\text{s}$. It also decimates along both time and frequency axes to Nyquist-sample the data from the correlator output. These values are the same as those of A15, and the compression process is described in more detail in Parsons et al. (2014). This compression process may imprint systematic biases in the data but those are not investigated in this work. After compression, data were first calibrated redundantly using logarithmic calibration and linear calibration techniques (Liu et al. 2010; Zheng et al. 2014; Dillon et al. 2018). An imaging-based flux density calibration was also applied using Pictor A fluxes derived from Jacobs et al. (2013).

The data are then grouped into bins according to local sidereal time. Within each bin, samples with modified z -scores above ~ 4.5 are flagged. As opposed to z -scores, which use a sample set’s mean and standard deviation to find outliers, modified z -scores use the median and median absolute deviation (MAD). Modified z -scores are discussed in more detail in Section 6 and thoroughly in Iglewicz & Hoaglin (1993). Data are binned into two sets, one containing odd-numbered days and the other even. These can then be differenced to estimate the noise and cross-multiplied for a power spectrum unbiased by noise.

2.3. Flagging and Subband Selection

We find that compared to all other antennas in the LST-binned data set, antennas 3 and 16 have an anomalously low number of samples. After LST binning, most baselines have samples from between 30 and the full 64 days in each frequency/time bin; baselines associated with antennas 3 and 16 contain bins with as few as 10 days sampled during the transit of Fornax A (~ 3 hr in the LST). In the interest of uniformity, these two antennas were therefore flagged and excluded from analysis. In a similar way, we limit the range of LSTs included in the final power spectrum to times that are sampled repeatedly throughout the observing

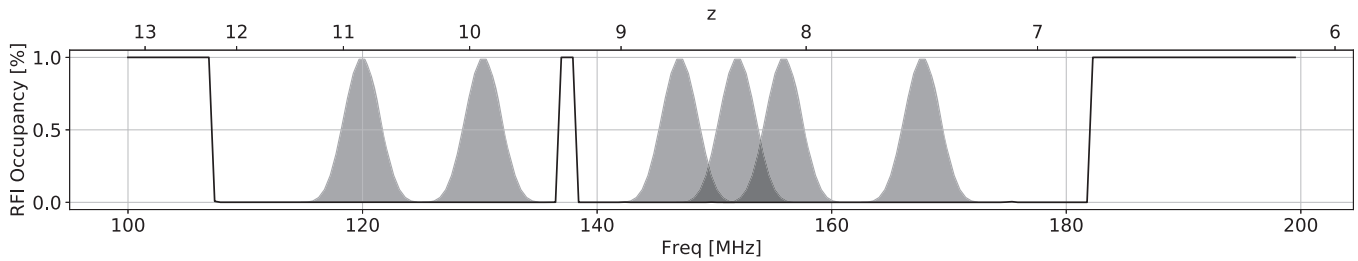


Figure 3. The six frequency bands used in this analysis plotted over the relative occupancy of flags from RFI. Redshift bands are denoted by the Blackman–Harris window functions used during the Fourier transform from frequency to delay in order to reduce foreground leakage to high delays. The specific windows chosen here are centered on $z = 10.87, 9.93, 8.68, 8.13,$ and 7.48 (119.7, 130.0, 146.7, 155.6, and 167.5 MHz respectively). Two subbands centered at 112 and 178 MHz could also be constructed with minimal RFI flagging; however, these bands contain significant high-delay systematics even after the application of the fringe-rate filter and provide little unique information both cosmologically and toward the identification of persistent systematics. The model of the beam is dominated by extrapolation in some or all of the frequencies in these subbands, and as a result, data products that depend heavily on the beam (the input simulation, thermal noise estimate, and input noise simulation) are not credible outside of the selected bands. Frequency bands used in this analysis include the 150 MHz, $z = 8.37$, band used in C18 and A15. This redshift bin is included in order to properly compare with previous works, but it is worth noting that the information obtained from this bin is not entirely independent from the two redshift bins with which it overlaps.

season, corresponding to a time window between LSTs $00^{\text{h}}30^{\text{m}}00^{\text{s}}$ and $08^{\text{h}}36^{\text{m}}00^{\text{s}}$.²⁴

The data are then divided along the frequency axis into smaller redshift bins for further power spectrum analysis. A practical limitation in redshift selection comes from a desire to avoid including channels with significant RFI flagging. Bands with the most continuous spectral sampling span the redshift range 11–7.5. We select redshift ranges that are approximately coeval, i.e., bandwidths over which limited evolution of the 21 cm signal is expected. To accommodate this constraint, we adopt a band size of 10 MHz.

This band size allows us to choose a number of spectral windows with very little to no RFI flagging. The specific windows chosen here are centered on $z = 10.87, 9.93, 8.68, 8.13,$ and 7.48 (119.7, 130.0, 146.7, 155.6, and 167.5 MHz respectively). These bands are illustrated visually in Figure 3. Two subbands centered at 112 and 178 MHz could also be constructed with minimal RFI flagging; however, these bands contain significant high-delay systematics even after the application of the FRF and provide little unique information both cosmologically and toward the identification of persistent systematics. The model of the beam is dominated by extrapolation in some or all of the frequencies in these subbands, and as a result, data products that depend heavily on the beam (the input simulation, thermal noise estimate, and input noise simulation) are not credible outside of the selected bands. As a validation check, we also include a reprocessing of the $z = 8.37$ bin centered at 151.7 MHz, which was analyzed in A15 and C18.

3. Noise Simulation

In parallel with the observed PAPER data, we process a simulation of thermal noise to help validate the simpleDS pipeline’s normalization, power spectrum estimation, and bootstrapped variance estimation techniques. To generate the input noise simulation, we assume that the per-baseline noise is drawn from a complex Gaussian distribution $\mathcal{CN}(0, \sigma_n)$. To determine the width, σ_n , of this distribution, we use the

radiometer Equations (9)–(15) from Clark (1999),

$$\sigma_n^2 = \frac{\text{SEFD}^2}{2\eta^2 \Delta\nu t_{\text{acc}}}, \quad (1)$$

where SEFD is the system equivalent flux density, η is the antenna efficiency, $\Delta\nu$ is the observing bandwidth in a frequency bin, and t_{acc} is the accumulation time of the observation.

The quantity SEFD/η is a measure of the expected variance of samples of the total noise power. Assuming the noise is Gaussian, the noise power is the variance of the underlying distribution, often described by a system temperature, T_{sys} . This quantity then is a measure of the variance of the sample variance of a Gaussian distribution, which equates to $\sigma_n^2 \propto 2T_{\text{sys}}^2$. This factor of 2 will cancel with the factor in Equation (1).

Substituting this into Equation (1) yields an expression for the variance of a realization of noise,

$$\sigma_n^2 = \frac{T_{\text{sys}}^2}{\Delta\nu t_{\text{acc}} N_{\text{days}}}, \quad (2)$$

where we added the term N_{days} to account for the averaging of individual samples during LST binning, assuming the noise is independent between days.

We assume that the system temperature, T_{sys} can be described by the relations from Rogers & Bowman (2008),

$$T_{\text{sys}} = 180 \text{ K} \left(\frac{\nu}{180 \text{ MHz}} \right)^{-2.55} + T_{\text{rcvr}}, \quad (3)$$

where we retain the parameters as measured or noted in past PAPER reports, most recently by A15: a sky temperature model of $T_{180} = 180 \text{ K}$ with a spectral index of $\alpha = -2.55$, a frequency-independent receiver temperature $T_{\text{rcvr}} = 144 \text{ K}$ (this parameter is taken from C18), a resolution of $\Delta\nu = 100 \text{ MHz}/203$ and an integration time $t_{\text{acc}} = 42.95 \text{ s}$.

Using Equation (2), we create a data set of Gaussian random noise matched in shape to the observed PAPER data. These simulated noise data are processed through simpleDS in parallel with the PAPER data.

²⁴ Note that the LST range here is slightly different from A15 but is identical to the one used in C18.

4. Simulated Sky

There are several challenges in making an accurate simulation of 21 cm instruments, ranging from the limited accuracy of catalogs to the computational challenges in simulating large fields of view and large bandwidths. A simulation of millions of sources from horizon to horizon over hundreds to thousands of channels and baselines is a formidable challenge. Simulators addressing these challenges include PRISim²⁵ (Thyagarajan et al. 2019), OSKAR²⁶ (Mort et al. 2010), FHD²⁷ (Sullivan et al. 2012), and to a limited extent CASA²⁸ (McMullin et al. 2007). The pyuvsim Python package (Lanham et al. 2019) is currently being developed to produce exactly such simulations as well.

Testing the power spectrum code on a foreground-only instrumental simulation can reveal internal inconsistencies, including scaling errors and other code errors; it can also help provide estimates of uncertainties in calibration and other sources of error. PAPER’s wide field of view ($\sim 45^\circ$ FWHM beam with significant sensitivity all the way to the horizon; Pober et al. 2012) drives a requirement for a simulation which does not employ flat-sky assumptions or approximations. One such simulator is PRISim, which performs a full-sky visibility calculation given lists of catalogs (Thyagarajan et al. 2015a, 2015b). Using PRISim, we generate ~ 8 hr of simulated PAPER data matching the observing parameters of the LST-binned data set.

The goal of this simulation is not to produce an accurate model of the sky suitable for subtraction or calibration, but rather to provide a sky-like input to the simpleDS power spectrum pipeline for power spectrum internal checks and rough comparison. The simulation can confirm the overall scale of our final power spectrum and helps identify sky-like modes which may leak outside of the horizon under a the delay transformation.

The sky model used by PRISim includes a GSM diffuse model (de Oliveira-Costa et al. 2008), point sources from the GLEAM sky survey with flux density > 1 Jy at 150 MHz (Wayth et al. 2015; Hurley-Walker et al. 2017), a model of Pictor A created from GLEAM, and a model of Fornax A created by using clean components derived from the deconvolution techniques described in Sullivan et al. (2012; R. Byrne & P. Carrol 2018, personal communication). This Fornax A model has a total flux of 541.7 Jy at 180 MHz, consistent with the low-frequency observations assuming a spectral index of -0.8 (McKinley et al. 2015). PRISim simulates diffuse emission as collections of Gaussian point sources, much like CLEAN components. The GSM component list is generated by interpolating the GSM HEALPix map to be oversampled by a factor of 4, and each pixel is then treated as an independent point source.

It is expected that this simulation will not perfectly reproduce the PAPER data, due not only to incompleteness in the sky model and imperfections in the instrument model, but also because of potential errors or approximations in the methodology simulation code itself (e.g., the choice to model the sky as made of point sources). To avoid the overinterpretation of the simulation results,

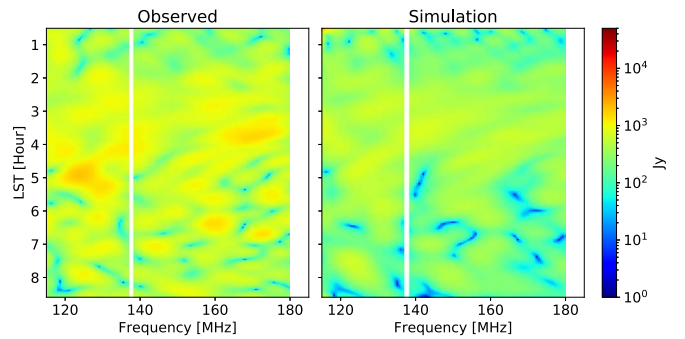


Figure 4. An LST–frequency plot of the amplitude of representative observed visibilities (left) and the PRISim simulation (right) for the ~ 8 hr of data analyzed in this work. While many details in the visibility amplitude structure do not match, there is general agreement, particularly near LST ~ 3 hr when Fornax A transits over the instrument.

we limit our use of PRISim foreground simulations to checking the flux scale (Section 4.2), understanding the impact of time averaging (Section 5.1.1), computing foreground error bar components (Section 7.1.3), constraining the general shape of the foreground power spectrum (Section 8), and establishing the expected change in foreground power with LST (Section 8.2.2).

4.1. Simulation Results

We begin the comparison of the input data and simulated PRISim data by noting that PRISim has, in the past, been primarily used to simulate delay power spectra rather than in the image domain; as such, we omit any detailed comparison of simulated phases with data. Similarly, the PRISim implementation of the PAPER beam has not been tested at a detailed level (for example, by imaging), and so delay modes near the horizon limit are not expected to be simulated as accurately as those well within the foreground wedge (see, e.g., Pober et al. 2016).

A comparison of the simulated and observed data is shown in Figure 4. Though some of the detailed fringing structures are not reproduced in the simulation, the relative shape of the fluctuations appear well matched between the two data sets. The overall amplitude, however, of the two data products differs significantly.

4.2. Absolute Calibration Check

One key question is the absolute calibration of the power spectrum amplitude scale. This scale combines a number of factors including the absolute calibration performed on the data described in Section 2.2, the conversion from Jansky to mK, the Fourier transform convention, and the cosmological scaling of delay modes. Each is relatively simple but important to check (for example, an error in h scales as h^3 on Δ^2).

Figure 5 shows the ratio of amplitudes between observed and simulated visibilities, averaged over redundant baselines. While both the observed and simulated data exhibit similar fringe patterns, the largest differences occur between LSTs of 5 and 7 hr. This is near the galactic anticenter and may be indicative of an incomplete sky model. The PAPER beam model used is a polynomial fit of the spherical harmonic coefficients (a_{lm}) fit from laboratory measurements taken between 120 and 180 MHz; beyond this range, the simulated data are excluded from further analysis.

²⁵ The Precision Radio Interferometry Simulator (PRISim) is publicly available at github.com/nithyanandan/PRISim.

²⁶ <https://github.com/OxfordSKA/OSKAR>

²⁷ <https://github.com/EoRImaging/FHD>

²⁸ <https://casa.nrao.edu/>

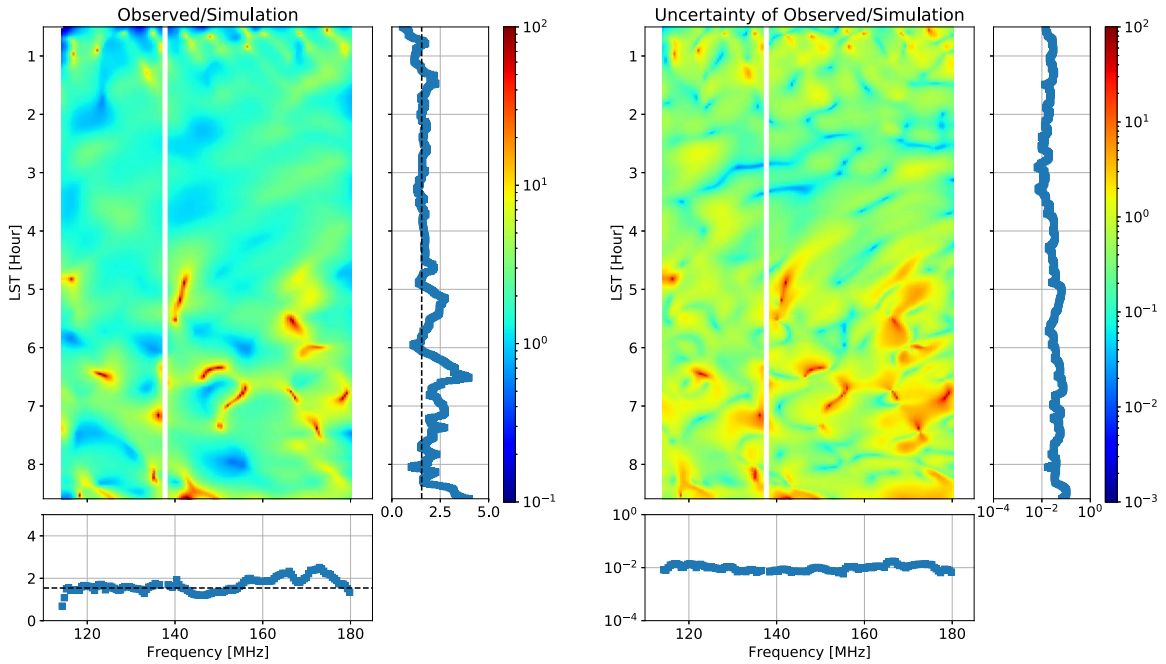


Figure 5. Ratio of the amplitude of the simulated to observed visibility (left) and the uncertainty of the ratio (right); notice the difference in color scales. The observed is obtained by an unweighted average over all baselines and the uncertainty from the variance across baselines. Also plotted are the mean of the ratio and uncertainty averaged along the time axis (bottom panel) and frequency axis (right panel) with the maximum likelihood scale factor overplotted (black dashed). While both the observed and simulated data exhibit similar fringe patterns, the largest differences occur between LSTs of 5 and 7 hr. This is near the galactic anticenter and could be indicative of an incomplete sky model. The most likely model scale factor is 1.54 ± 0.04 at 95% confidence.

The ratio also becomes large where interference between fringing sources drives the visibility amplitudes close to zero, but overall the ratio is generally close to unity. These zero crossings make a mean value difficult to interpret; here we make a best estimate by computing the likelihood of a range of scale values (g) given the baseline to baseline variation,

$$\log \mathcal{L}(g) = \sum_{\nu, t, \text{bl}} \frac{-(g * V(\nu, t)_{\text{sim}} - V(\nu, t)_{\text{bl}})^2}{2 * \text{var}(V(\nu, t)_{\text{bl}})}, \quad (4)$$

where the subscript “bl” refers to a unique redundant group, and the variance ($\text{var}(V(\nu, t)_{\text{bl}})$) is computed over all baselines in a redundant group.

The scale factor is fit over the domains [0.5, 4.5] hr in LST when the foreground simulation fringe pattern shows the most agreement with the observed visibilities and over the frequencies [120, 180] MHz where the PAPER beam model is most reliable.

The maximum likelihood scale factor is 1.54 ± 0.04 at 95% confidence. This is consistent with the ratio observed during the first half of the data set in LSTs 1h to 5h (the dashed line plotted in Figure 5). This scaling factor is used when estimating the expected foreground signal in Section 7.1.3 and as an overall scaling factor on the power spectrum estimated from the simulated data in Section 8.

4.2.1. Model Scale Discussion

The 50% difference in scale between the model and the data is notable enough to merit further discussion. There are many possible sources for this difference, including uncertainty in catalog inputs to the PRISim simulator, the instrument model itself, the calibration of the PAPER data, or some combination of all three. Deeper investigation requires careful testing of

each component separately, work that is beyond the scope of the present study. However, it is worth reviewing some of these aspects.

The original absolute calibration reported in A15 was done by imaging the Pictor field (at LST = 4 hr) in each channel, correcting for a primary beam model and fitting a Gaussian to the extracted Pictor A source. This was done in 10 minute snapshots with the resulting spectra averaged together. The standard deviation of the flux estimate was of order ~ 25 Jy at 68% confidence on each channel. A similar scale variation seen from channel to channel was consistent with sidelobe confusion. The change in scale due to that effect was on the order of a few percent.

The difference could also be attributed to the calibration of the simulator. Work is in progress to better verify the accuracy of array simulation codes; lacking firm conclusions, we only expect PRISim simulations of diffuse structure to be accurate in amplitude to within a factor of 2 (Thyagarajan et al. 2015a).

Because the flux calibration of the simulations has not been rigorously independently tested, and the flux scale for the data is tied to a well-established model in Jacobs et al. (2015), we scaled the simulation to match the data. The flux calibration in this paper is thus unchanged from A15.

5. Analysis Pipeline Comparison

In this section, we describe the differences in the analysis steps prior to Fourier transform and power spectrum estimation between this work and A15: the time averaging and foreground removal techniques (see Figure 1).

5.1. Time Averaging

The LST-binned data were initially averaged into 43 s bins, a timescale that is short compared to the ≈ 3500 s fringe

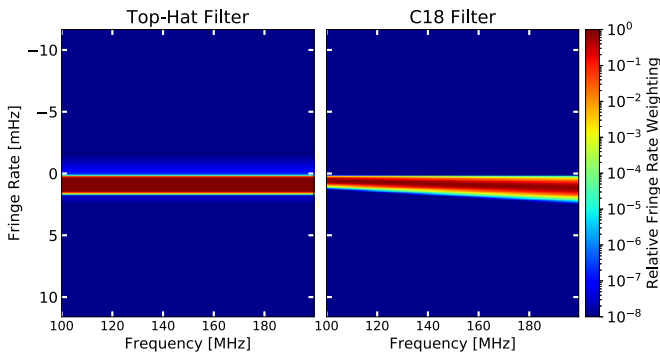


Figure 6. Comparison of the top-hat fringe-rate filter (TH, left) and the filter used in C18 (right) in the fringe-rate–frequency domain. The C18 filter varies with frequency, and this spectral variation can cause additional structure when performing a delay transform of the visibilities. In the interest of simplicity in this analysis, we choose to perform time averaging with the TH filter.

coherence time of the 30 m baselines (see Section 3.5 in A15). Here, as in past PAPER analyses, we choose to perform additional time averaging by convolving the time stream with a windowing function. This function is defined as a filter in fringe-rate space (the Fourier dual to LST), which can be tuned to maximize sensitivity to sky-like modes and exclude slowly varying systematics. Parsons & Backer (2009) showed that a fringe rate corresponds to sky-like rates of motion which map geometrically to a great circle on the sky. Parsons et al. (2016) then showed that an FRF can be defined with weights corresponding to the square root of the instrument’s primary beam power squared and integrated along the line of constant fringe rate. Applying an FRF with this weighting provides optimal thermal sensitivity in power spectrum estimation.

Previous PAPER analyses have used variations on such a filter. A15 formed the beam-weighted filter, fitted a Gaussian in fringe-rate space, and then artificially increased the width of the Gaussian to provide easy parameterization across the PAPER bandpass and decrease the effective time integration. A similar Gaussian fit was also used and discussed in C18, but the width of the fit was not increased in this analysis.

However, as can be seen in the right-hand side of the top of Figure 6, this filter is frequency dependent. In particular, the maximum fringe-rate range probed by a baseline increases linearly with frequency. This spectral dependence may introduce additional structure during the delay transform; further investigation is needed to find the best approach for mitigating this effect.

Additionally, the use of these “aggressive” FRFs has also been shown to contribute to signal loss (C18) especially when used in conjunction with quadratic power spectrum estimators.

While QE formalism is not used in this work, as a simplification to avoid potential signal loss and reduce contamination of high-delay modes, we adopt a top-hat filter that weights all fringe rates evenly across frequency, similar to the filter used in Parsons et al. (2012b). The maximum fringe rate passed by our filter is set by the highest frequency included in the data set; the lowest fringe rate passed is chosen to exclude known common-mode signals with zero fringe rates. This results in an effective integration time of ~ 940 s measured as the equivalent noise bandwidth of the windowing function. While the filter results in suboptimal thermal sensitivity on the estimated power spectrum, it is designed to remove a common-mode signal observed in previous PAPER

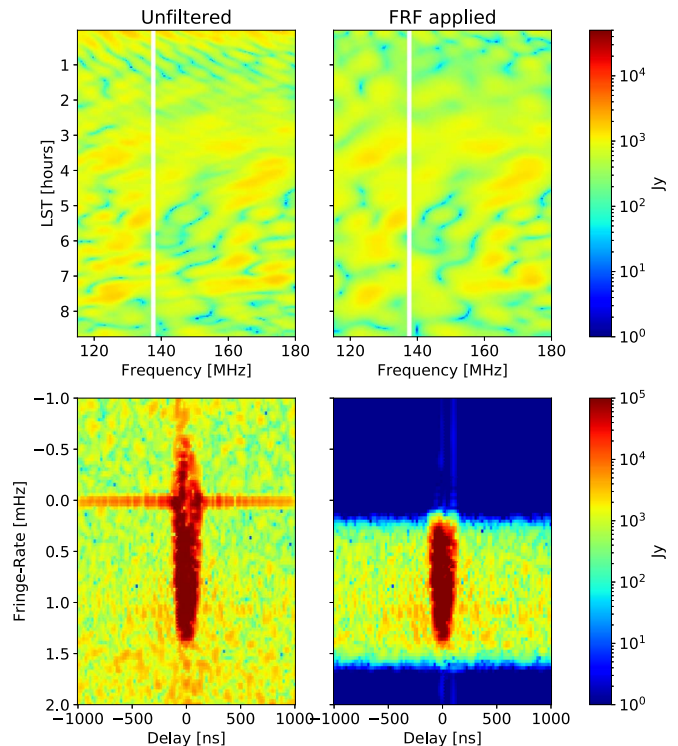


Figure 7. Top: LST and frequency waterfalls of representative baselines taken from the even LST-binned set before (left) and after (right) application of the top-hat FRF. The baseline illustrated is the antenna pairs (1, 4). The application of the fringe-rate filter removes very fast fringe modes but preserves the structure of sky-like modes. Bottom: the same baseline before (left) and after (right) the application of the FRF plotted in fringe rate and delay space. The Fourier representation of the data illustrates the common mode at fringe rate = 0 mHz suppressed by the filter.

analyses while providing a moderate increase in thermal sensitivity.

5.1.1. Common Mode

Past PAPER analyses have noted signals that vary on timescales longer than would be expected from an ideal interferometer (Ali et al. 2015). Such common modes²⁹ are excluded here by setting the minimum fringe rate included in the filter to 3.5×10^{-5} Hz; this excludes all modes with periods longer than ~ 45 minutes.

Suppressing slowly or negatively fringing sources will suppress sources with elevations at or below the south celestial pole. These modes are generally low in the $\sim 45^\circ$ PAPER primary beam. When applying this filter to our foreground simulation, the total simulated power is observed to decrease by 7.97%; as a result, we apply a correction factor of 1.086 to our power spectrum estimates and their uncertainties to account for the associated signal loss.

Waterfall plots of a representative baseline before and after the application of the fringe-rate filter are shown in Figure 7. The application of the FRF removes very fast fringe modes but preserves the structure of eastward-moving sky-like modes. Also visible is the common mode at fringe rate = 0 mHz, which is suppressed by the the application of the FRF. Without

²⁹ Previously referred to as “crosstalk.” These common-mode signals may not necessarily result from signals observed in one antenna and leaked to another (a time-delayed sky signal) but rather any time-independent signal that is observed by all antennas.

filtering, the common mode would create a strong bias at high-delay modes during power spectrum estimation.

5.2. Foreground Removal

To mitigate foreground contamination during power spectrum estimation, PAPER analyses have used a WIDA often referred to as a “clean-like” iterative deconvolution algorithm. This algorithm relies on the underlying mathematics of CLEAN as described in Högbom (1974) to remove delay components from PAPER data inside of some range of delays. This type of deconvolution and its specific application to radio data are described in Parsons & Backer (2009). The WIDA was used in Parsons et al. (2012b, 2014), Jacobs et al. (2015), A15, Kerrigan et al. (2018), and C18.

The use of this filtering technique has been omitted from this analysis. While the technique should not affect cosmological signals outside the user-defined range of delays to clean (Parsons & Backer 2009; Parsons et al. 2012b, 2014, and explored further in Kerrigan et al. 2018), recent works have also shown the use of this filter does not produce a statistically significant reduction of power at high-delay modes (Kerrigan et al. 2018). Because our analysis aims to focus on upper limits set at high-delay modes, we omit this step in the interest of simplicity. Even without any attempt to remove foregrounds from the visibility data, we find that our delay transform used to estimate the cosmological power spectrum is not limited by the inherent dynamic range of the transform.

6. Redundancy of PAPER Baselines

Before estimating the power spectrum of the data, we conduct statistical tests on the observations to determine the delay to which the baselines are redundant. The per-baseline delay spectrum estimation technique described in Parsons et al. (2012b) can be averaged across all baseline cross-multiples only for perfectly redundant baselines.³⁰ While it is unrealistic to assume that the PAPER baselines are perfectly redundant, this analysis can help identify extreme outliers which should not be used in the power spectrum estimation.

As discussed in Section 2.1, the 8×8 antenna configuration used in the PAPER-64 deployment was chosen to increase sensitivity on baselines with many redundant observations. Each of the three baseline vectors are sampled many times across the grid-like array. Rather than averaging baselines together (as was done in previous PAPER analyses for computational simplicity), we cross-multiply all redundant pairs and then bootstrap-average for an estimate of the variance. This is described in more detail in Section 7.1.1.

A first test of the array’s redundancy is to compare the measured variation between baselines with that expected due to thermal noise, using the input noise simulation discussed in Section 3.

As a measure of variance between baselines, we take the MAD of the visibility amplitude across redundant baselines for each frequency and time, defined as

$$\text{MAD}(t, \nu) = \text{median}(|V_{i,j}(t, \nu)| - \text{median}(|V(t, \nu)|)), \quad (5)$$

where the median visibility amplitude is taken at each time and frequency across the redundant baseline group.

³⁰ Or if the nonredundant component of an ensemble of baselines is described by a random variable with mean 0 (like Gaussian noise).

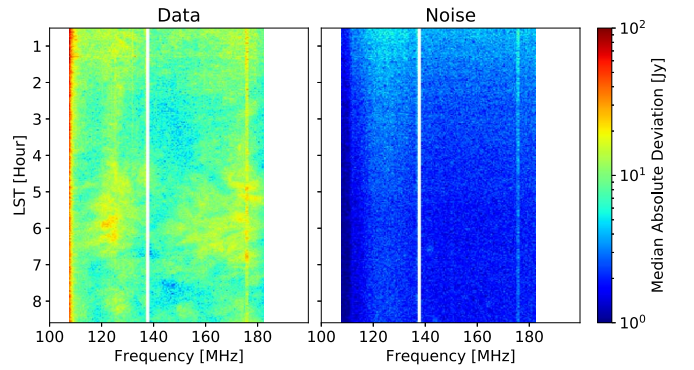


Figure 8. A representative median absolute deviation (MAD) for both data (left) and noise simulation (right) computed for each time and frequency observed by PAPER in the LST range $00^{\text{h}}30^{\text{m}}00^{\text{s}} - 08^{\text{h}}36^{\text{m}}00^{\text{s}}$. The data shown here corresponds to strictly east–west baselines in Figure 2. For perfectly redundant sky measurements, the individual baseline measurements will only differ by thermal noise. The large amplitude of the deviations observed illustrates that there is a significant amount of nonredundant information in the data.

The MAD for both data and our noise simulation is shown in Figure 8. For perfectly redundant sky measurements, the individual baseline measurements will only differ by thermal noise. Some frequency–time pairs have an MAD consistent with thermal noise; however, the larger deviations observed at other frequencies and times illustrate a significant amount of nonredundant information in the data.

We then use the MAD to estimate the significance of each baseline’s deviation from the median baseline measurement using the modified z -score ($M_z(t, \nu)$) defined as

$$M_z(t, \nu) = 0.6745 \frac{|V_{i,j}(t, \nu) - \text{median}(V(t, \nu))|}{\text{MAD}}, \quad (6)$$

which can be thought of as the number of “sigmas” each data point is away from the median. The 0.6745 scaling factor is introduced to normalize the modified z -score for a large number of samples (Iglewicz & Hoaglin 1993).

These scores, M_z , are calculated for each set of LST-binned data (even and odd). In order to provide an estimate of a single M_z for every baseline, the modified z -scores are initially averaged in quadrature of the LST day dimension. The histograms of these modified z -scores averaged in quadrature over LST day for both the input data and noise simulation are shown in the left-hand side of Figure 9. A quadrature average is chosen to identify absolute outliers as opposed to an unweighted averaged, where a hypothetical baseline with an even distribution of positive and negative outliers could average to zero.

The distribution of modified z -scores for all frequencies and times illustrates a significance of nonredundant signal beyond the contributions from thermal fluctuations. To better identify the baselines (or antennas) contributing to this nonredundant information, a quadrature average is performed over the frequency and time dimensions for all baselines, and the resulting distribution is shown in the right-hand side of Figure 9.

Because the noise simulation is a model of perfect redundancy, the quadrature averaging produces a very narrow distribution centered near 1. As a result, it is impossible to remove only a small number of outlier baselines (or antennas)

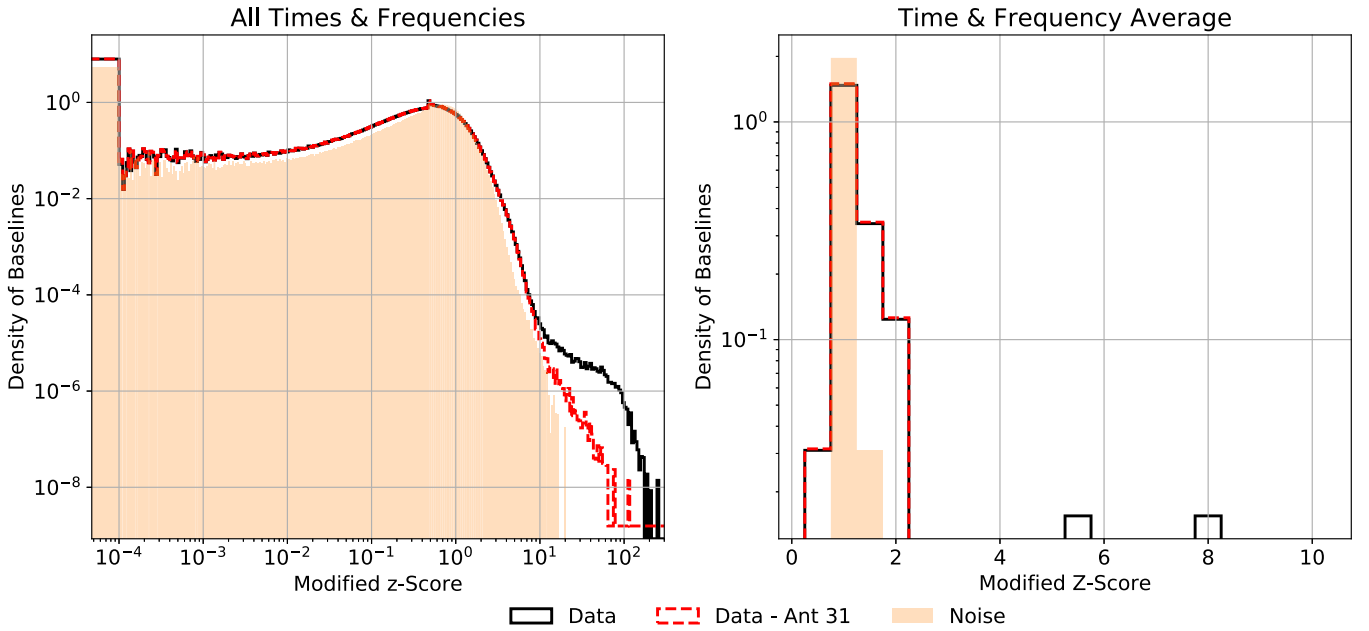


Figure 9. A histogram of modified z -scores of data averaged in quadrature over LST day (even/odd; black line) and input noise simulation also averaged over LST day (orange) before (left) and after (right) averaging in quadrature over frequencies and times. Also plotted is the distribution of z -scores after removing any identified outliers (dashed red). The visual shoulder in the left-hand plot near $M_z \sim 50$ is evidence of nonredundant contributions larger than the fluctuations from thermal noise. To identify the contaminating baselines, a quadrature average of the frequency and time axes is performed to produce a single modified z -score per baseline. The variance of the distribution of the noise is ~ 40 times smaller than the distribution from the data. As such, performing a statistical cut based on the distribution of the noise simulation would result in removing $\sim 85\%$ of all baselines. This is a result of the noise simulating a perfectly redundant set of baselines. Therefore, a visual inspection is necessary to identify potential outliers. The two baselines (21, 31) and (31, 45) present as obvious candidates for removal. Both baselines have modified z -scores greater than 4 and removing them is consistent with a cut at $M_z = 3.5$ as suggested in Iglewicz & Hoaglin (1993). The removal of these two baselines also flags antenna 31 entirely from the analysis as it contributes only to these baselines.

using a cut based on the distribution of scores from the noise simulation. The variance of the distribution of the noise is ~ 40 times smaller than the distribution from the data. As such, performing a statistical cut based on the distribution of the noise simulation would result in removing $\sim 85\%$ of all baselines. This redundancy analysis is aimed to only remove the worse antenna (or two) from the analysis, not drastically reduce the number of input baselines. Therefore, a visual analysis of the distribution of modified z -scores is necessary to identify potential outliers.

The two baselines (21, 31) and (31, 45) present as obvious candidates for removal. Both baselines have modified z -scores greater than 4, and removing them is consistent with a cut at $M_z = 3.5$ as suggested in Iglewicz & Hoaglin (1993). The removal of these two baselines also flags antenna 31 entirely from the analysis as it contributes only to these baselines. The distribution of modified z -scores without this outlier antenna is also plotted in Figure 9.

Although no other baselines qualify as outliers, the difference in distributions between the data and noise simulation indicates an amount of nonredundancy significantly inconsistent with thermal noise fluctuations from the baselines in this analysis and may affect the interpretation of our final power spectrum estimates.

7. Power Spectrum Estimation

Our analysis pipeline uses a delay-based power spectrum estimation technique first developed in Parsons et al. (2012b). The highly redundant baseline configuration in PAPER provides high thermal sensitivity on a small subset of short (~ 30 m) baselines by observing repeated samples of the same sky signals

with independent noise (Parsons et al. 2012a). Also, the fringe spacing corresponding to the baselines and observing frequencies probe a single spatial fluctuation scale (k_{\perp} -mode) as a function of frequency. By Fourier-transforming along the frequency axis into delay space, foregrounds are expected to be constrained to an area bound by the maximum geometric delay of the chosen baseline (Parsons et al. 2012b). Additionally, Kerrigan et al. (2018) showed that an application of foreground subtraction applied to delay-based power spectrum estimators only affects delay modes just outside of the geometric delay limit of a baseline. As such, thermal sensitivity at delay modes larger than the maximum geometric delay of a baseline should be unaffected whether or not foregrounds are subtracted. The high thermal sensitivity and constrained foreground in delay space make PAPER well suited for a delay-based power spectrum estimation.

The power spectrum of the 21 cm emission can be estimated directly from interferometric visibilities following Parsons et al. (2012a, 2014):

$$P(k_{\parallel}, k_{\perp}) = \left(\frac{\lambda^2}{2k_B} \right)^2 \frac{X^2 Y}{\Omega_{\text{eff}} B_{pp}} \langle \tilde{V}_i^*(\tau, t) \tilde{V}_j(\tau, t) \rangle_{i \neq j, \text{LST}}, \quad (7)$$

where λ is the observed wavelength, $X^2 Y$ converts from interferometric units to cosmological units, k_B is the Boltzmann constant, Ω_{eff} is the effective area of the primary beam depending on the units of the input visibility (Parsons et al. 2014, 2016), $B_{pp} = \int d\nu |\phi(\nu)|^2$ is the effective bandwidth of the power spectrum estimation where $\phi(\nu)$ is the spectral taper function used during Fourier transformation, and $\tilde{V}_i(\tau, t)$ is the delay-transformed visibility observed by baseline i . This formula assumes the baselines over which the delay transform

is taken have a minimal change in length over the bandwidth of the transform. This allows for a one-to-one correspondence between the delay modes as a function of τ and the cosmological modes, k_{\parallel} (Liu et al. 2014a).

The power spectrum is estimated by selecting subsets of available bandwidth, weighting by a tapering function ($\phi(\nu)$) to improve dynamic range, delay-transforming visibilities with an FFT, cross-multiplying different baseline pairs, and then bootstrap-averaging cross-multiplication pairs. Foreground leakage in the FFT is minimized with a Blackman–Harris (BH) tapering function before the Fourier transform over frequency. The BH window does induce a correlation between directly adjacent Fourier modes, however, and the resulting bandwidth/redshift range sampled by each power spectrum window is effectively halved for each redshift band.

These steps are implemented with the publicly available simpleDS³¹ Python package. This package and analysis pipeline have been developed specifically to provide a simple alternate analysis to other pipelines that take more aggressive strategies with regard to weighting and foreground removal.

7.1. Power Spectrum Uncertainties

In this section, we present several different methods for estimating the uncertainties on our power spectrum estimates. Combined, these alternative approaches help provide a consistent picture of the uncertainties on our results.

7.1.1. Bootstrapped Variance

Power spectrum errors can come from thermal, instrumental, and terrestrial (RFI) sources. Biases and additional variance can also be unintentionally introduced in analysis steps (e.g., calibration, time averaging). Those with a known covariance (like thermal noise) can be propagated through the data processing and power spectrum estimation steps into an analytically estimated error bar. The other sources are harder to estimate from first principles. However, the total variance of the data—*independent of the exact source of error*—can be estimated by bootstrapping: estimating the power spectrum from subsets of data and then calculating the variance of these estimates. In the redundant PAPER array, the axis most amenable to bootstrapping is the selection of baseline pairs which are cross-multiplied to get a power spectrum.

We provide an overview of the bootstrapping technique used in this work below. This method incorporates the bootstrapping revisions described in more detail in Section 3.2.2 of C18. Specifically, we perform the power spectrum estimation by cross-multiplying all pairs of baselines within a redundant set and between the two even and odd LST-binned data sets described in Section 2. These cross-multiplications are then randomly sampled with replacement and then averaged over all cross-multiple products, resulting in a single waterfall of power spectra. An average is then taken across the LST axis to form a single power spectrum versus delay.

We repeat this process by selecting different baseline cross-multiplications to find new realizations of the power spectrum. The variance of these bootstrap samples is interpreted as the uncertainty in the power spectrum estimate. This bootstrap estimation is designed to probe the underlying distribution of

allowed values given our observed values (Efron & Tibshirani 1994; Andrae 2010).

7.1.2. Thermal Variance

Liu et al. (2014a, 2014b) showed that when estimating the power spectrum in the regime $k_{\parallel} \gg k_{\perp}$, the delay axis (the Fourier dual to frequency) can (to a good approximation) be reinterpreted as the cosmological k_{\parallel} axis. Under this assumption, to provide a theoretical estimate of the thermal variance, we use the expected noise power derived in Parsons et al. (2012a) and applied in Pober et al. (2013, 2014) and C18:

$$P_N(k) = \frac{X^2 Y \Omega_{\text{eff}} T_{\text{sys}}^2}{t_{\text{int}} N_{\text{days}} N_{\text{bls}} N_{\text{pols}} \sqrt{2 N_{\text{1st}} N_{\text{sep}}}}, \quad (8)$$

where $X^2 Y$ converts from interferometric units to cosmological units, T_{sys} is the system temperature, Ω_{eff} is the effective size of the primary beam in steradians (Parsons et al. 2014), N_{1st} is the number of independent LST samples, N_{pols} is the number of polarizations used in the analysis, t_{int} is the integration time of an LST sample, N_{days} is the effective number of days used in LST binning, N_{bls} is the effective number of baselines combined, and N_{sep} is the number of independent baseline types. See C18 for a thorough definition of all the terms in this thermal noise estimate.

This estimate assumes that the number of times each LST is observed is the same number of times across the full course of the season, when in practice LSTs were observed between 5 and 60 times (a consequence of only observing at night with a drift-scanning telescope). These counts are tabulated during the LST binning process. If the noise is constant from night to night, an effective N_{days} can be calculated by averaging the inverse sum of squares over the sidereal period as described in Jacobs et al. (2016). The observations here yield an effective integration length varying between 27 and 29 days depending on the redshift bin.

As an aid to future repeatability, the values used here are listed in Table 1 and the calculation is documented as a Python module called 21CMSSENSE_CALC available at github.com/dannyjacobs/21cmsense_calc.

Equation (8) is an analytic form that serves as a useful “sanity check” on the expected noise levels, but is not expected to be highly accurate in the absence of simulations to calibrate its terms. Simulation of T_{sys} through the power spectrum pipeline (the noise input described in Section 3) is likely to be the most robust estimate of thermal noise errors.

7.1.3. Foreground Error Bars

The propagation of the thermal error above does not fully capture the variance expected on modes with significant non-noise-like power (i.e., foregrounds). To demonstrate this fact, let us assume each visibility, $\tilde{V}_i = s + n_i$, to be the sum of a signal component, s , and some noise term, n_i . Assuming the signal component is constant across all baselines and $n_i \sim \mathcal{CN}(0, \sqrt{P_N})$ is independent on every baseline i , we show in Appendix that the variance of each power spectrum cross-multiple can be written as

$$\sigma_{P(k)}^2 \equiv \text{Var}(P(k)) = 2P_s(k)P_N + P_N^2, \quad (9)$$

where $P_s(k)$ is the true power spectrum of the sky signal and P_N is the noise power spectrum from Equation (8).

³¹ github.com/RadioAstronomySoftwareGroup/simpleDS

Table 1
PAPER-64 Theoretical Noise Estimate Values

Term	Description	Value in Redshift Bin						Units
		10.87	9.93	8.68	8.37	8.13	7.48	
X^2Y	Conversion from interferometric (u, v, η) to cosmological $(k_{\perp,x}, k_{\perp,y}, k_{\parallel})^a$	578.77	533.36	471.06	454.90	442.58	408.52	$\frac{\text{Mpc}^3}{h^3 \text{sr Hz}}$
Ω_{eff}	Effective beam area ^b	1.645	1.664	1.489	1.487	1.496	1.580	sr
T_{sys}	System temperature	653.37	556.33	446.75	422.31	404.69	360.30	K
T_{rcvr}	Receiver temperature			...144...				K
N_{lst}	Number of effective LST samples			...31...				
N_{sep}	Number of independent baseline types ^c			...3...				
t_{int}	Integration time of LST sample ^d			...938...				s
N_{days}	Number of effective days used in LST binning	27.63	27.81	28.07	28.33	28.44	28.79	
N_{pols}	Number of polarizations combined in analysis			...2...				
N_{bls}	Number of effective baselines			...47...				

Notes.

^a This value is also a function of the assumed background cosmology. See Furlanetto et al. (2006) and Liu et al. (2014a) for more information.

^b The effective beam area is influenced by the choice of fringe-rate filter applied (Parsons et al. 2016). The computation for this value is also found in Appendix B of Parsons et al. (2014).

^c The ‘‘sep’’ subscript refers to the separation of antennas on the PAPER-64 grid. These separations are what define the different baseline types described in Figure 2.

^d This value is computed as the equivalent noise bandwidth (ENBW) of the FRF applied to the data. See C18 and Parsons et al. (2016) for more information.

The signal noise cross-term in Equation (9) will dominate delay/ k modes inside the horizon where the expected foreground signal exceeds thermal noise levels. At the highest delay/ k modes, the uncertainty will be dominated by the thermal variance.

Here we use the simulated PRISim observation as a rough estimate of $P_s(k)$, with the simulation scaled to match the data on average across the entire band,

$$P_s(k) = g^2 P_{\text{PRISim}}(k), \quad (10)$$

where g is the model scale factor computed in Section 4.

7.1.4. Comparison of Power Spectrum Uncertainties

As an internal consistency check, we compare the sizes of the bootstrapped uncertainties to the analytical thermal noise and simulated foreground uncertainties. This comparison is made by taking the ratios of each type of uncertainty, which is plotted in Figure 10.

As a basic test, we see that the bootstrap variation of the external noise simulation (plotted in orange) is never further than a factor of 0.7 away from the theoretical prediction of purely thermal noise. Considering the 10^9 dynamic range spanned by power spectrum values and remembering that the theoretical error bar includes several approximations, a 30% worst-case difference is within expectations.

Bootstrapped error bars of the data are significantly larger than the purely thermal variance, sometimes reaching $10^5 \times$ larger in the horizon and nearly $5 \times$ the thermal noise at the highest redshifts in what, according to the simulations, should be noise-dominated bins. In general, the overly large error bars seemingly trace out all areas where the mean power spectrum itself manifests a notable excess.

However, accounting for the PRISim-simulated foreground terms in the expected variance in the denominator of this ratio, agreement increases by orders of magnitude (the dashed curve), with the largest discrepancies now only a factor of ~ 10 . The remaining disagreement is concentrated in the modes where

simulations show the weakest foreground amplitude that is still detectable above the noise. This remaining discrepancy at $|\tau| \sim 400$ ns may be sourced from an incomplete sky model.

The addition of simulated foreground power to the noise calculation accounts for the largest discrepancies in error estimation; however, it does not decrease the discrepancy at high delays. At redshifts 8.68 and below, the difference between the calculated error estimates, the bootstrapped errors, and the noise simulation all generally agree. However, in the two highest redshift bins, the bootstrapped error estimate remains roughly $2 \times -5 \times$ larger. In all subsequent analyses, we include all three noise estimates as useful comparisons.

8. Multiredshift Power Spectrum Results

Figure 11 shows the delay power spectrum estimates for all three of our principal products: the observed data (black), the PRISim-simulated observation (blue), and the noise-only simulation (orange). Within delay modes between $\sim \pm 400$ ns, both the observed and simulated data illustrate similar shapes. This suggests that the statistically significant detections of power observed in PAPER immediately outside the horizon limits are consistent with foreground signals (as suggested by the study of foreground subtraction applied to PAPER data in Kerrigan et al. 2018). At larger delays, however, the PAPER power spectra are a mix of statistically significant detections and null results. The most statistically significant detections at high delays are seen to occur at the lowest frequencies.

8.1. Evaluation of FRF

The effectiveness of the FRF in downweighting contaminating delay modes, can be evaluated after performing power spectrum estimation.

The power spectrum estimates before and after the application of the FRF are shown in Figure 12. While the application of the FRF provides some improvement in thermal noise, it also provides suppression of the highly significant detections at delays $|\tau| > 400$ ns. These detections are

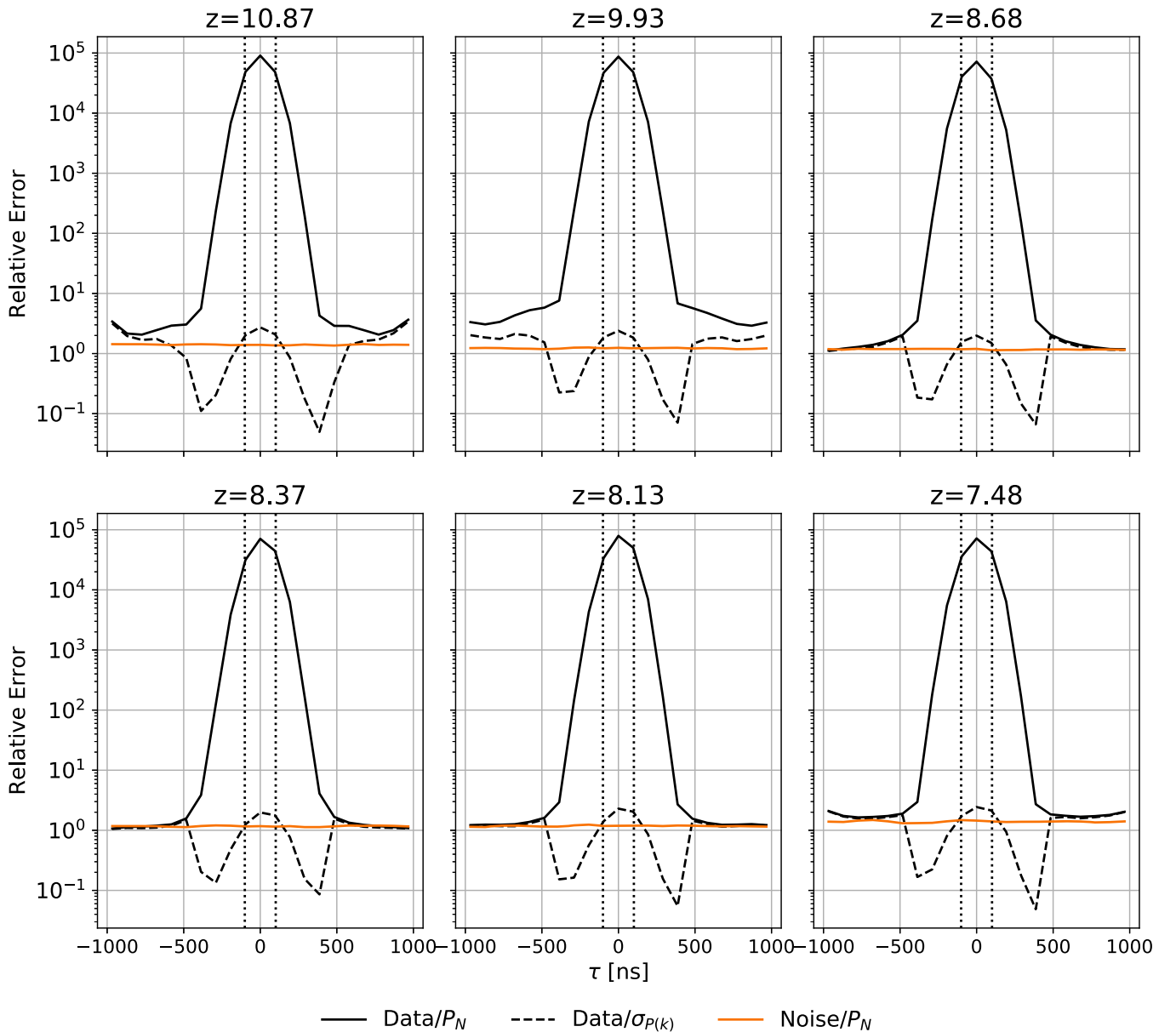


Figure 10. The ratio of the bootstrap error bars of both data and noise to estimates of the predicted uncertainties for each redshift bin. Panels are ordered such that redshift increases toward the upper left. A ratio helps to compare different estimates of power spectrum error bars together. Bootstrapped errors of simulated noise (orange) over $P_N(k)$ (Equation (8)) are very close to unity ratio, an important consistency check. The ratio of data variance to $P_N(k)$ (solid black line) is nearly unity like at high delay but is $10^4 \times$ higher where the simulated foregrounds dominate (refer to Figure 11 to identify these regions). Accounting for the foreground-dependent term in the theoretical error bar in the ratio denominator (dashed black line, $\sigma_{P(k)}$; Equation (9)), agreement is improved by three orders of magnitude, with the largest discrepancies now only a factor of 10 in the modes with the weakest foreground amplitude. This order of magnitude of disagreement outside the horizon at $|\tau| > 100$ ns may be the result of an incomplete sky model.

inconsistent with the expected leakage from the simulated foreground signal (also filtered with the FRF) and are signatures of the common mode described in Section 5.1.1 and also visible in Figure 7.

Even for less aggressive filters than the ones used in A15 and C18, filtering can significantly reduce systematic contamination during the delay transformation. The choice of the shape of filters is contingent on the acceptable amount of signal loss. As described in Section 5.1.1, when applying this filter to our foreground simulation, the total simulated power is observed to decrease by 7.97%; as a result, we apply a correction factor of 1.086 to our power spectrum estimates to account for the associated signal loss.

8.2. Investigation of High-delay Detections

In this section, we present several analyses designed to help determine the cause of the remaining statistically significant detections at high delays seen in the PAPER observations.

8.2.1. The Imaginary Power

The power spectrum is computed by cross-multiplying different baseline pairs within redundant groups. Ideally, this cross-multiplication of complex-valued delay spectra will result in any sky-like power being confined to the real part in the power spectrum, leaving the imaginary part dominated by noise. However, effects can leak real sky power into the

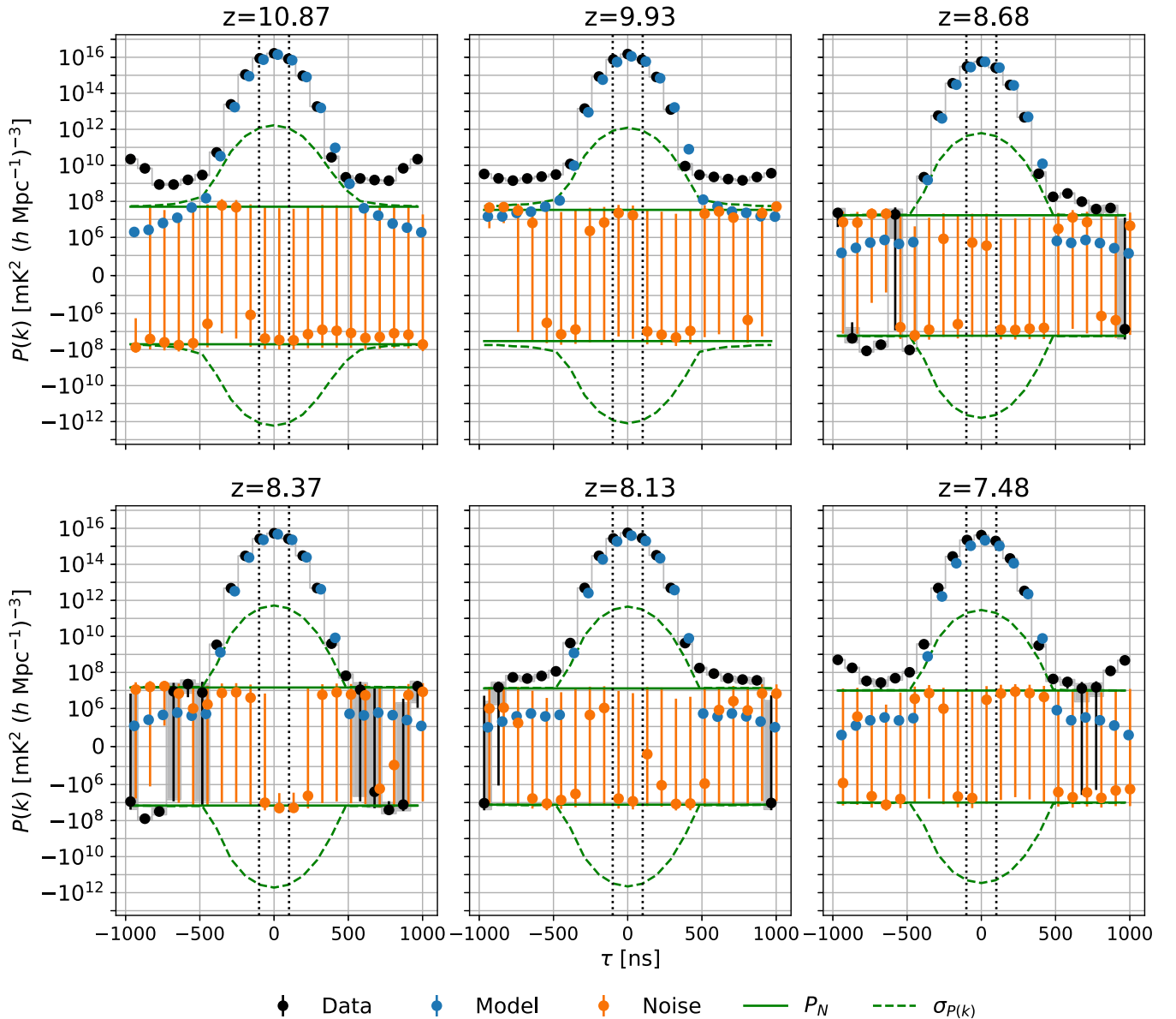


Figure 11. Power spectrum estimates computed for the observed data (black), simulated noise (orange), and simulated observation (blue). Error bars on points are the bootstrapped uncertainty. The solid green line indicates the theoretical thermal noise estimate for each redshift bin, and the dashed green line includes the foreground error from Equation (9). Gray shaded regions are the foreground-dependent uncertainties plotted around each data point. The vertical black dotted lines indicate the horizon/wedge/light travel time for a 30 m baseline. As shown in Figure 10, the simulated noise is consistent with the theoretical thermal noise predictions. At delay $\tau = 0$ ns, both the data and PRISim simulation show good agreement in the total power observed; generally, the power at all delays inside the horizon agrees between the two simulations within a factor of ~ 5 . The simulated data set also shows some power leakage outside the horizon, consistent with the power observed by PAPER out to ≈ 400 ns. The PAPER data also show numerous statistically significant detections beyond 400 ns, however, which are not predicted by the PRISim simulation. To investigate the origin of these signals, multiple jackknives and null tests are performed as described in Section 8.2.2.

imaginary part of the power spectrum. A perfectly calibrated array with nonredundant baselines—for example, with slightly different antenna positions—will cause two nominally “redundant” baselines to have slightly different phases. The imaginary parts of these cross-multiplied visibilities will therefore not cancel out, and nonzero power will be seen in the imaginary component of the power spectrum estimate. The same effect would come from a perfectly redundant but imperfectly calibrated array. It is also important to note that because of the foreground-dependent error bars derived in Section 7.1.3, imaginary power should increase at low delay, though continue to be consistent with zero. In a sense, the amount of statistically significant power in the imaginary

component of the power spectrum, compared to power in the real part, is a measure of the net redundancy and calibration quality of the array.

A comparison of the real and imaginary parts of the power spectrum is shown in Figure 13. The statistically significant imaginary components at $|\tau| < 400$ ns are generally at a power level, which is $\sim 20\%$ of the real components at the same delay. All the detections in this region are also biased to negative power levels. This may result from nonredundancies in calibration or baseline orientation.

At delay modes $|\tau| > 400$ ns, the imaginary component of the power spectrum displays comparable power to the real part. This is especially prominent in the two highest redshift bins,

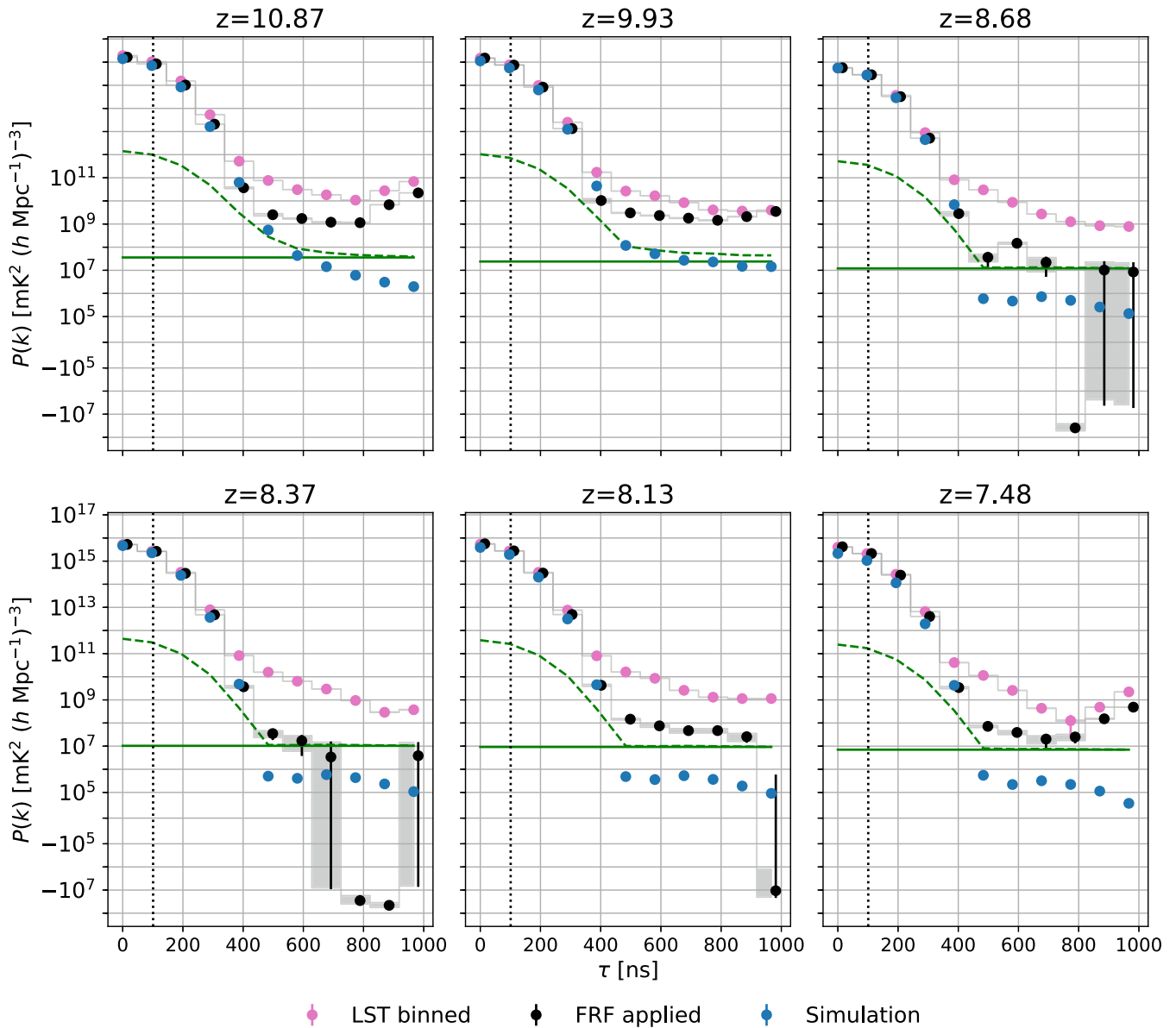


Figure 12. The estimated power spectrum value before (purple) and after (black) application of the fringe-rate filter. The simulated data points (blue) have also been filtered with the FRF (the same as in Figure 11). All other points and lines are the same as Figure 11. While the application of the fringe-rate filter provides some improvement in thermal noise, it also provides suppression of the highly significant detections at delays $|\tau| > 400$ ns. These detections are inconsistent with the expected leakage from the simulated foreground signal (blue) and are signatures of the common mode described in Section 5.1.1.

but is observable across the entire band. The disagreement between the imaginary component and the foreground-dependent thermal uncertainty is indicative of some non-redundant information, systematic biases introduced by data analysis or calibration steps, or residual contaminants like improperly flagged RFI

8.2.2. Null Tests

While the imaginary power suggests at least some presence of calibration error or nonredundancy, it does not fully explain the origin of the excess power at delays greater than 400 ns. Calibration errors, as long as they do not introduce spectral structure, should not necessarily scatter power to high delays. Null tests—i.e., differences between power spectra of different data selections—can provide hints of the origin of these detections.

For example, differencing the power spectra of two distinct stretches of sidereal time will remove isotropic cosmological signals³² but leave signals with strong dependence on sidereal time (like foregrounds). Dividing the data set in half by LST into ranges $[00^{\text{h}}30^{\text{m}}00^{\text{s}}, 04^{\text{h}}30^{\text{m}}00^{\text{s}})$ and $[04^{\text{h}}30^{\text{m}}00^{\text{s}}, 08^{\text{h}}36^{\text{m}}00^{\text{s}})$ creates two sets of roughly equal sensitivity. The resulting differenced power spectrum is shown in Figure 14, along with a matching calculation for the foreground simulation. The two are broadly consistent at delays less than 400 ns, i.e., they have the same sign and a similar amplitude. Galactic synchrotron emission and bright point sources (like Fornax A and Pictor A) are the most obvious contenders for strong variability. We also see that the significant power seen in

³² Cosmological signals can only be removed through this method up to cosmic variance. However, because thermal uncertainties dominate the cosmic variance, it is a decent approximation for this work.

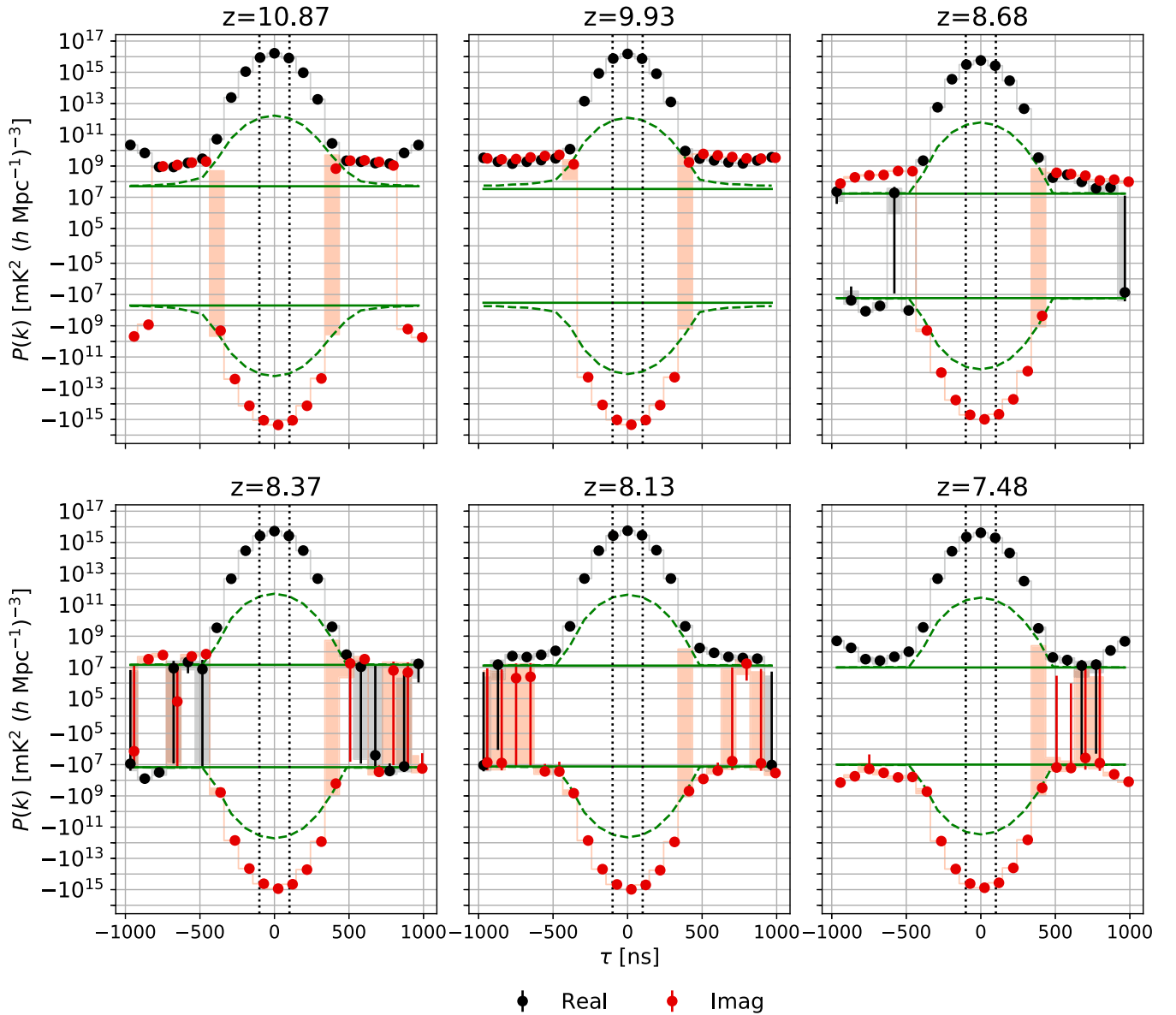


Figure 13. The real (black) and imaginary (red) components of the power spectrum of PAPER data. The red shaded region is the foreground-dependent theoretical error bar drawn around the imaginary components; all other lines are the same as in Figure 11. There are statistically significant imaginary components at $|\tau| < 400$ ns, generally at a power level that is $\sim 20\%$ of the real components at the same delay. All of the detections in this region are also biased to negative power levels. This may result from nonredundancies in calibration or baseline orientation. At delay modes $|\tau| > 400$ ns, the imaginary component of the power spectrum displays comparable power to the real part. This is especially prominent in, but not isolated to, the two highest redshift bins. The statistically significant imaginary power is indicative of some nonredundant information during power spectrum estimation, systematic biases introduced during data analysis or calibration, or residual contaminants like improperly flagged RFI.

modes well beyond the horizon (for example, the strong positive offset at redshift 9.93 seen in the Figure 11 power spectrum) is reflected in this null test.

We also see that the imaginary component of the power spectrum null test is comparable to the real component at most delay modes across all redshifts. This suggests a sidereal time dependence of phase differences between baselines. In particular, note that the strong bias seen at redshift 9.93 is associated with a strong imaginary bias, implying a phase rotation between baselines. Such an LST dependence of the imaginary component might be expected for nonredundancy (slightly different sky seen by nominally redundant baselines) or repeatable differences in calibration which depends on the sky configuration (for example, one calibration solution when Fornax is transiting and a different one for when Pictor

dominates). This kind of variation in redundant calibration with sky flux density was shown in Joseph et al. (2018). Variations in calibrations from ionospheric fluctuations can also impact power spectrum estimation by introducing spectral structure and nonredundant information (Cotton et al. 2004; Intema et al. 2009). This picture of nonredundancy strengthens the earlier hints provided by Section 6’s z -score analysis, which suggested that redundancy was particularly low around 120–130 MHz (redshifts 9 and 10).

A second easily constructed null test is to difference power spectra made from only the even and odd binned data sets. Recall that these sets were constructed by separating even- and odd-numbered days during the LST binning. A significant difference in this test would be suggestive of a variation at the night-to-night level, which departs significantly from the mean,

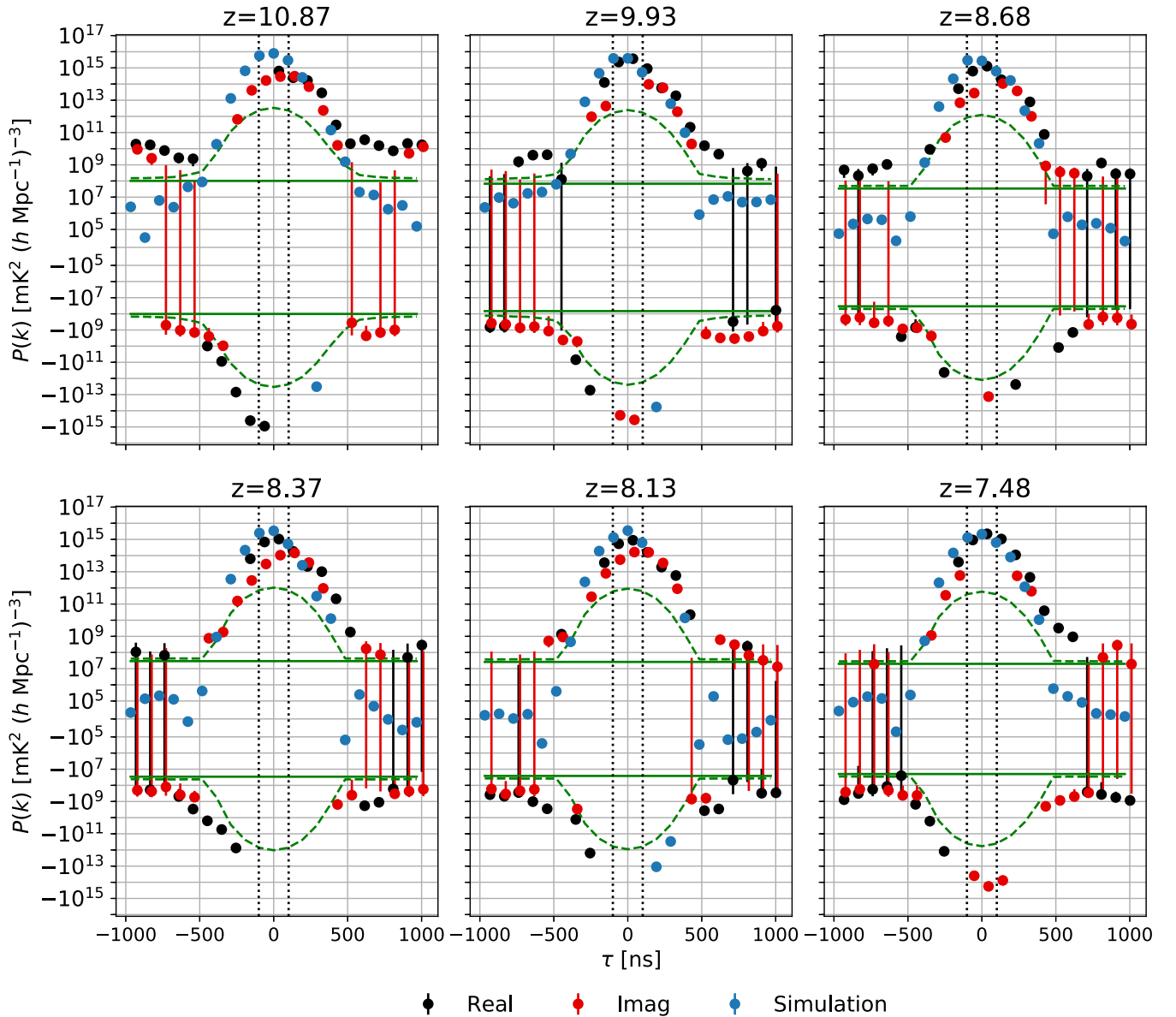


Figure 14. Null tests constructed by splitting the LST range ($00^{\text{h}}30^{\text{m}}00^{\text{s}}$, $08^{\text{h}}36^{\text{m}}00^{\text{s}}$) in half (at $04^{\text{h}}30^{\text{m}}$), making two power spectrum estimates, and differencing the result. Real (black) and imaginary (red) are both shown, along with the null-test results when applied to the simulated data (blue). Such a difference would remove isotropic cosmological signals, leaving anything with dependence on sidereal time. Noise curves are as described in Figure 11. Statistically significant detections in the real part suggest power varying across the sky while significant imaginary power suggests a time dependence to phase-calibration errors. The observed variations are consistent with simulation up to delays of 400 ns. The detections’ higher delay modes indicate large LST dependence, which is inconsistent with cosmological power.

as these two sets are otherwise expected to have identical sky signals with different realizations of noise.

The resulting differenced power spectra for each redshift band are shown in Figure 15. Across all redshifts, there are points well beyond the horizon which are inconsistent with both the analytic purely thermal variance and the foreground-dependent uncertainty. However, there are two important differences from the LST null test. First, the overall amplitude of the difference power spectrum is much less. Within the horizon, the difference amplitude is at most a few $\times 10^{13}$, or less than 0.1% of the power spectrum. Second, the imaginary power spectrum is consistent with uncertainty across most modes. This is particularly notable within the horizon where even a small percent difference would drive a significant deviation. This suggests that whatever causes the small but detectable difference between even and odd is not attributable to a phase difference between baselines. A variation

in calibration as a function of JD can also cause the excess at delays less than 400 ns: days calibrated with the same solutions, but actually possessing some night-to-night gain variations, will result in some nonredundant signals between days.

The two highest redshift bins again show the most significant differences at high delay; the observed power values in this test are comparable to or even exceed the power spectrum estimates shown in Figure 11, and the imaginary leakage is 10% of that. This result may provide evidence of a signal contaminating a single day that is averaged into the LST-binned data set, which is suppressed during the cross-multiplication of days during power spectrum estimation. Examples of such a systematic are improperly flagged RFI, a low-amplitude signal not detected before cross-multiplication, or a large transient gain isolated to a single night.

Another interesting feature can be seen in the redshift 8.68 bin in Figure 15. Here we see a consistent bias which was not

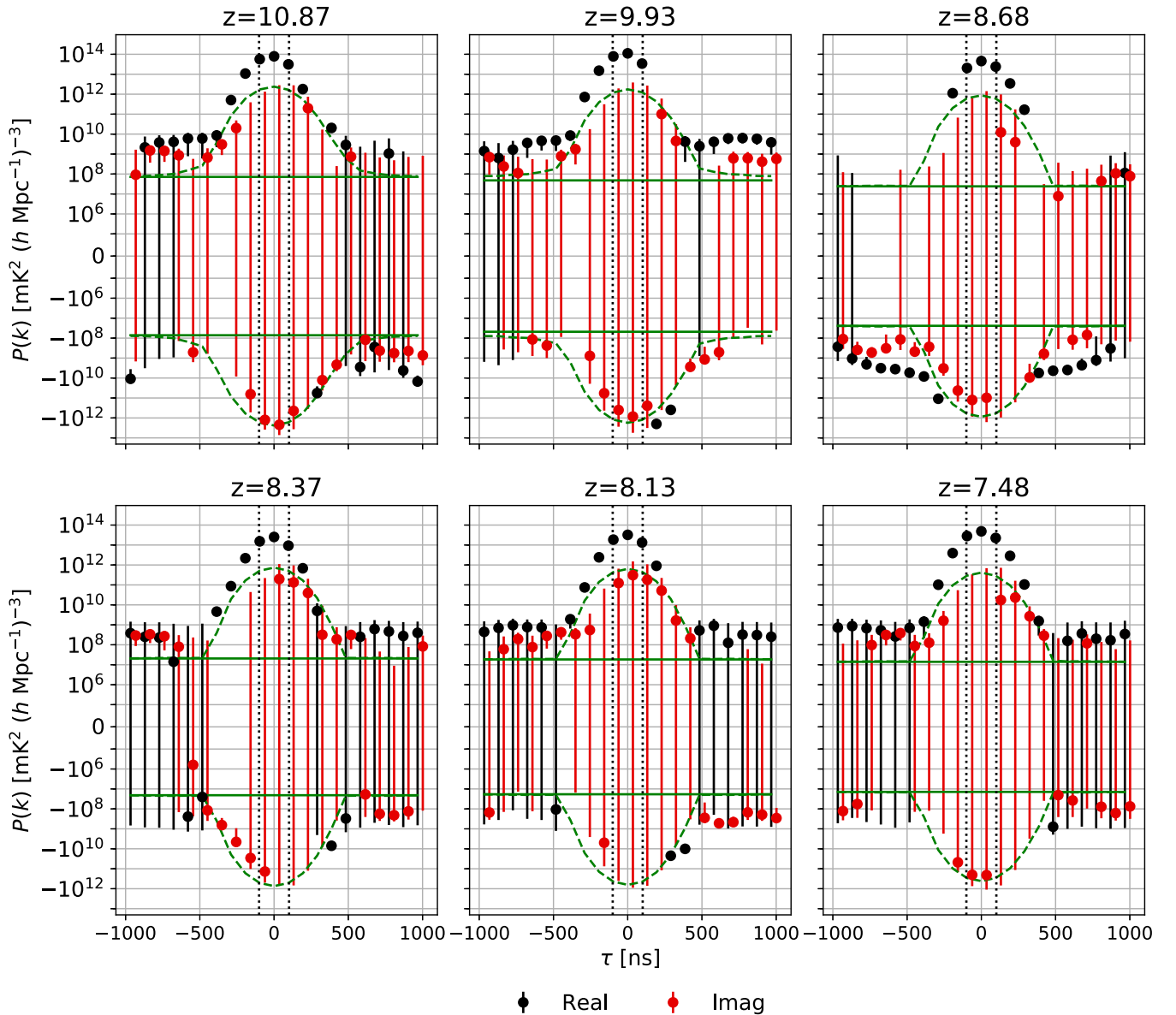


Figure 15. In the LST binning process, data were split and binned into sets containing only even- or odd-numbered days; plotted here is the difference between the power spectra from these two sets. We use the same color scheme as Figure 14. Where the largest difference in the LST null test (Figure 14) was on the order of 10% of the measured value, here differences are less than 1% at delays less than 400 ns, and the imaginary points are nearly all consistent with the predicted error bars. At delays larger than 400 ns, statistically significant detections in the three highest redshift bands are at comparable levels to the power spectrum values in Figure 11. This may be the result of contamination in only one set of the even or odd data (positive values for even, negative values for odd) which is mitigated during the cross-multiplication of these sets during power spectrum estimation. A variation in calibration as a function of JD can also cause the excess at delays less than 400 ns: days calibrated with the same solutions, but actually possessing some night-to-night gain variations, will result in some nonredundant signals between days.

present in the mean power spectrum (Figure 11). However, there is a similarly shaped bias in the imaginary part of the mean power spectrum. A plausible hypothesis is that, in this part of the spectrum, phase error between baselines is larger in one of the even/odd LST-binned sets than the other. However, there is no clear significant difference in redundancy seen in the z -score/MAD analysis, so further evidence would be required to support this conclusion.

8.2.3. Null-test Discussion

Our two null tests provide evidence that the foregrounds, which vary significantly as a function of LST, are likely the cause of some of the residual power detected at high delays

during power spectrum estimation. There is also some evidence that suggests significant phase differences exist between nominally redundant baselines, which introduce nonredundant signals into the power spectrum estimates.

The presence of highly significant detections in the even-odd null test also suggests there may be some net nonredundant signal between the two LST-binned data sets. These points are significant compared to the propagated error bar ($\sim 10\sigma$ to $\sim 100\sigma$ inside the horizon) but represent a small fraction of the total power observed ($\leq 1\%$ of the power in Figure 11). However, the agreement of the imaginary part of the power spectrum with the foreground-dependent error bar suggests that each of the even-odd sets has internally redundant baselines but the data sets themselves are slightly different.

Both the null tests discussed in this work and the presence of a significant fraction ($\sim 20\%$) of power leaking from the real to the imaginary component of the power spectrum indicate the presence of nonredundant and non-isotropic signals. The latter is not surprising because this analysis is performed on data with no foreground subtraction, and the sky varies with LST as the galaxy and strong point sources rise and set over an observation. In some places, particularly at low frequencies, this power couples to larger delays, presumably because of instrumental spectral structure. The even–odd null test suggests that this spectral structure potentially varies in time while the imaginary component suggests that the spectral structure is not the same across nominally redundant baselines.

8.3. Possible Future Directions

8.3.1. Jackknives in LST Binning

An additional jackknife could be used to identify and possibly remove residual RFI and night-to-night variations identified in the even–odd null test. The variation is significant enough to be observable after differencing data averaged over the entire season. If a specific night is the source of this result, it could potentially be further tracked down with additional jackknives with smaller sets of binned days or by performing a null test by differencing data from the first and second half of the observing season. This would provide information about the stability of antennas and observations over the life of the PAPER experiment. Unfortunately, returning to the initial raw visibility data set is outside the scope of this analysis.

8.3.2. Beam Null Test

Nonredundancy happens when baselines, which in theory should see the same sky, in fact measure slightly different skies. Two obvious ways for this to happen are variations in antenna position and variation in beam pattern. In theory, an element like PAPER should produce a symmetric beam, though this is not true in practice. A simple test for nonredundancy due to beam differences would be to test for deviations from symmetry by recording observations with antennas rotated by 180° . Differencing the 0° and 180° data sets would highlight abnormalities in the beam response to the sky between antennas. For an ideal, symmetric beam, all sky signals will cancel and leave thermal noise fluctuations at all times; however, imperfections in beam response will not cancel, resulting in a net signal in the visibility data. Characterizing these net signals can help inform more precise beam models and place constraints on the level of beam-to-beam variation between different antennas.

9. 21 cm Upper Limits

We use the PAPER data to place upper limits on the 21 cm signal strength using the dimensionless power spectrum: $\Delta^2(k) = (|k|^3/2\pi^2)P(|k|)$. To convert from interferometric delay to cosmological comoving wavenumber, we assume *Planck* 15 cosmology. These power spectra are shown in Figure 16.

As a summary and comparison of progress across the field, we also report, from each published power spectrum, the lowest upper limits in each redshift band, shown in Figure 17. This minimum is taken across the k ranges reported by each experiment to be free of possible signal loss or other extraneous

factors (for example, early PAPER results reported values inside the filtered wedge but indicated they were not to be used).

To encapsulate the results of this work, the most sensitive limit is reported from the range $0.3 < k < 0.6 h \text{ Mpc}^{-1}$, where both null tests pass for most k modes in each redshift bin. These limits on the 21 cm power spectrum from reionization are $(1500 \text{ mK})^2$, $(1900 \text{ mK})^2$, $(280 \text{ mK})^2$, $(200 \text{ mK})^2$, $(380 \text{ mK})^2$, and $(300 \text{ mK})^2$ at redshifts $z = 10.87$, 9.93 , 8.68 , 8.37 , 8.13 , and 7.48 , respectively. Table 2 also provides a summary of this data.

These upper limits represent a significant increase compared to prior limits published by the PAPER instrument (a factor of ~ 10 in mK). They also exceed the expected amplitude of a fiducial 21CMFAST³³ model by a factor of ~ 100 in mK (Mesinger et al. 2011). These limits supersede all previous PAPER results for reasons described in C18.

10. Conclusion

We reanalyzed the PAPER-64 data first presented in A15 and presented 21 cm power spectra and uncertainties in five independent redshift bins. These estimates are made using an independently developed pipeline which skips foreground subtraction and simplifies time averaging. Simulations of noise and foregrounds are used to build a basic picture of internal consistency. The resulting power spectra reach the noise limit across much of the spectrum but above redshift 9 (below 130 MHz), they demonstrate a statistically significant excess of power. Null tests support a picture where these power spectrum detections are caused by foregrounds modulated by spectrally dependent deviations from redundancy or calibration error. In particular, the z -scores and imaginary power tests suggest that residuals could be the result of some net nonredundant signal between baselines in a nominally redundant group.

Future analyses of highly redundant sky measurements will require strict comparisons between nominally redundant samples before cross-multiplication to ensure effects like these can be mitigated. Also, further jackknives and comparisons of data should be done before or as part of LST binning to detect likely contributions to excess. They will also require more precise antenna placement to ensure baselines designed to be redundant do not introduce signal in the imaginary component of the power spectrum.

These results represent the most robust results from the PAPER experiment and supersede all previous PAPER power spectrum limits. This includes results both from PAPER-32 (Parsons et al. 2014; Jacobs et al. 2015; Moore et al. 2017), which used a different covariance estimation technique but have not been subjected to a rigorous reanalysis à la C18, and previous PAPER-64 results (Ali et al. 2015, 2018). Any constraints on the spin temperature of hydrogen made by Pober et al. (2015) and Greig et al. (2016) based on the previously published upper limits should also be disregarded. Though these measurements do not place significant constraints on the IGM temperature, the analysis presented in these two papers remains relevant to any future limits on the 21 cm power spectrum at levels similar to the original results of A15.

The current best limits from 21 cm power spectrum experiments are shown in Figure 17. To date, all power spectrum estimates have been reported as upper limits.

³³ github.com/andreimesinger/21cmFAST

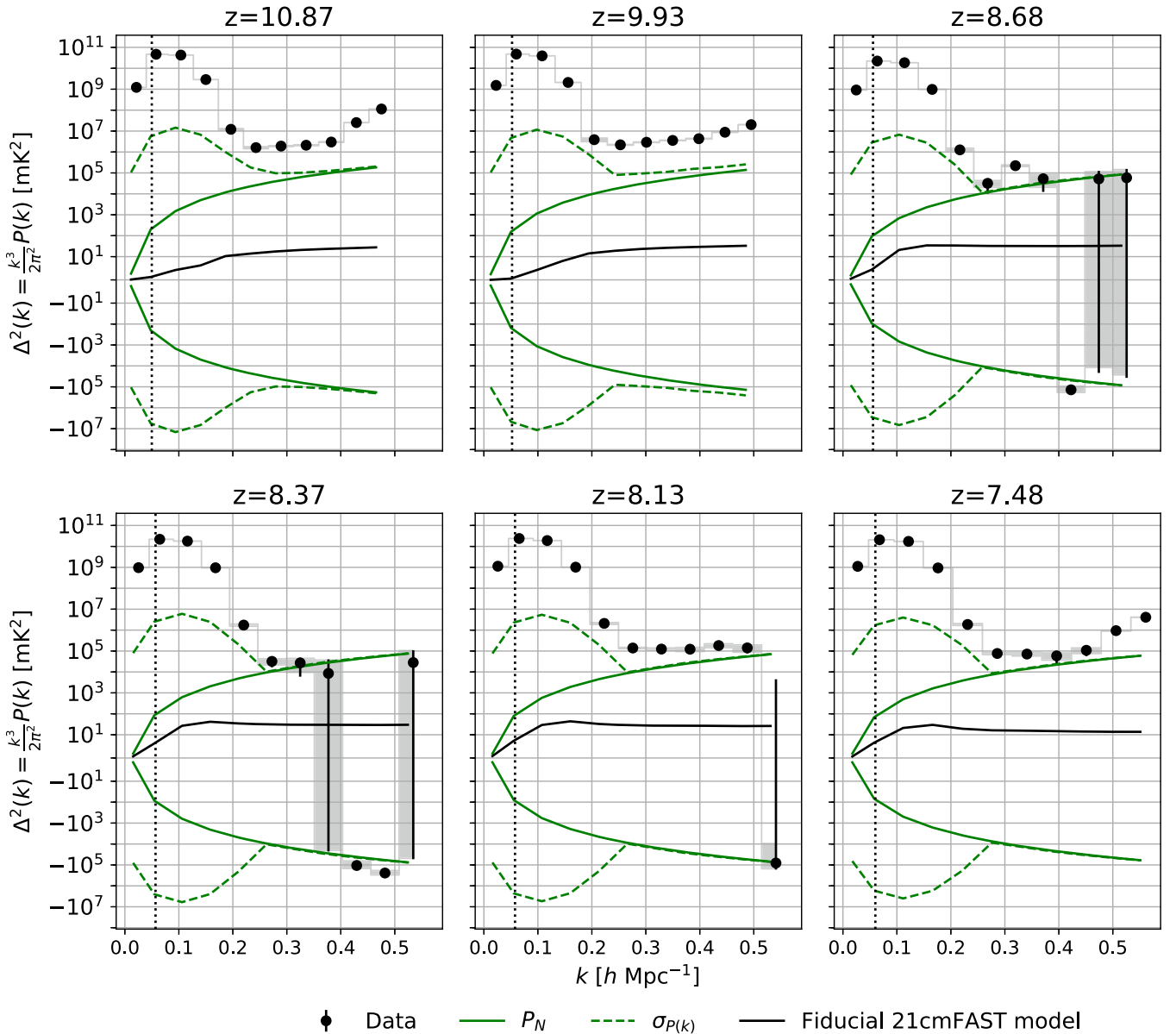


Figure 16. The dimensionless power spectrum ($\Delta^2(k) = (k^3/2\pi^2)P(k)$) estimates and their uncertainties derived from the PAPER-64 observations. All error bars represent 2σ uncertainties. Also plotted are the theoretical thermal noise limits from Equation (8) (solid green) and the foreground-dependent variance estimate from Equation (9) (dashed green line). These are the same lines as in Figure 11 with the addition of the black solid line representing fiducial 21cmFAST models of reionization for comparison. The horizon line (vertical dotted black) has been transformed from the maximum signal delay between antennas to the cosmological comoving size scales using Equations (12) and (13) of Liu et al. (2014a).

However, to discern and characterize the physics of reionization, high-significance detections of the 21 cm power spectrum are necessary. Next generation radio telescopes, like the fully realized 350 element configuration of HERA (Pober et al. 2014; DeBoer et al. 2017; Liu & Parsons 2016) and the future Square Kilometre Array (SKA; Mellema et al. 2013), are predicted to be able to make these detections and put stringent constraints on reionization.

We would like to thank Adam Beardsley, Judd Bowman, Bryna Hazelton, and Miguel Morales for their insightful discussions. We would also like to thank Ruby Byrne and Patti Carroll for supplying extended source models of Fornax A and Pictor A.

This work made use of the following python software packages: pyuvdata (Hazelton et al. 2017), astropy (Astropy Collaboration et al. 2013), scipy (Jones et al. 2001), and numpy (Oliphant 2006).

Some of the results in this paper have been derived using the HEALPix (Górski et al. 2005) package.

M.J.K. is supported by the NSF under project number AST-1613973 and would also like to acknowledge the support of Arizona State University. C.C. would like to acknowledge the UC Berkeley Chancellors Fellowship, National Science Foundation Graduate Research Fellowship (Division of Graduate Education award 1106400). PAPER and HERA are supported by grants from the National Science Foundation (awards 1440343, and 1636646). A.R.P., D.C.J., and J.E.A. would also like to acknowledge NSF support (awards 1352519, 1401708, and 1455151, respectively). S.A.K. is supported by the University of Pennsylvania School of Arts and Sciences Dissertation Completion Fellowship. A.L. acknowledges support from a Natural Sciences and Engineering Research Council of Canada (NSERC) Discovery Grant and the

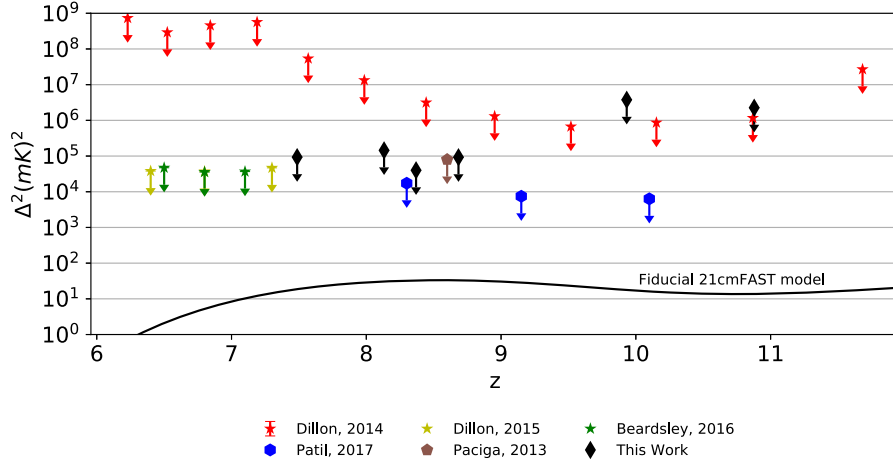


Figure 17. A comparison of the lowest limits achieved by various instruments in the k ranges reported by each instrument. The results reported from this paper are taken in the range $0.3 \leq k \leq 0.6 \text{ h Mpc}^{-1}$. Data are taken from the MWA (stars; Dillon et al. 2014, 2015; Beardsley et al. 2016), the GMRT (pentagon; Paciga et al. 2013), LOFAR (hexagons; Patil et al. 2017), and PAPER (diamonds; this work). We include the $z = 8.37$ redshift bin analyzed both here and in C18, although it is worth noting this redshift bin is not entirely independent from the $z = 8.13$ and 8.68 bins, as can be inferred from the overlapping window functions from Figure 3. For reasons described in C18, these PAPER results should supersede all previous PAPER limits.

Table 2

The Minimum Volume-weighted Power Spectrum Estimates $\Delta^2(|k|)$ (mK)² from This Analysis Computed over the Range $0.3 < |k| < 0.6$

Redshift	$ k $ (h/Mpc)	$\Delta^2(k)$ (mK) ²	$\delta\Delta^2(k)^a$ (mK) ²
7.49	0.39	5.6×10^4	3.5×10^4
8.13	0.32	1.2×10^5	2.0×10^4
8.37	0.37	1.0×10^4	3.2×10^4
8.68	0.36	3.8×10^4	4.1×10^4
9.93	0.34	3.5×10^6	1.9×10^5
10.88	0.33	2.1×10^6	1.5×10^5

Note.

^a All uncertainties are 2σ .

Canadian Institute for Advanced Research (CIFAR) Azrieli Global Scholars program. G.B. acknowledges the Rhodes University research office, funding from the INAF PRIN-SKA 2017 project 1.05.01.88.04 (FORECaST), the support from the Ministero degli Affari Esteri della Cooperazione Internazionale —Direzioe Generale per la Promozione del Sistema Paese Progetto di Grande Rilevanza ZA18GR02 and the National Research Foundation of South Africa (grant No. 113121) as part of the ISARP RADIOSKY2020 Joint Research Scheme. This work is based on the research supported in part by the National Research Foundation of South Africa (grant No. 103424). We would also like to thank SKA-SA for site infrastructure and observing support.

Software: simpleDS (github.com/RadioAstronomySoftwareGroup/simpleDS), pyuvdata (Hazelton et al. 2017), scipy (Jones et al. 2001), numpy (Oliphant 2006), astropy (Astropy Collaboration et al. 2013), PRISim (Thyagarajan et al. 2019).

Appendix A Foreground-dependent Variance

To find the variance of $P(k)$, begin by assuming each visibility $\tilde{V}_i(\tau, u, v, w) = s + n_i$ is the sum of the true sky signal, s , and a noise component, n_i .

For convenience, define the cosmological conversion factor

$$\Phi = \left(\frac{\lambda^2}{2k_B} \right)^2 \frac{X^2 Y}{\Omega_{pp} B_{pp}}. \quad (11)$$

Also for simplicity in this analysis, we ignore cosmic variance in the signal term. This results in the signal term being not a random variable but related to the power spectrum of the sky by $s^2 = P_s(k)/\Phi$, where $P_s(k)$ is the true power spectrum of the sky signal for a delay-transformed visibility. Let the noise term be drawn from the complex distribution $n_i \sim \mathcal{CN}(0, \sqrt{P_N(k)/\Phi})$, where n_i is independent for each baselines.³⁴

Then, we can propagate the variance in $P(k)$ as

$$\sigma_{P(k)}^2 = \text{Var}(P(k)) = \text{Var}(\Phi \langle \tilde{V}_i^*(\tau, t) \tilde{V}_j(\tau, t) \rangle_{i \neq j, \text{LST}}) \quad (12)$$

$$= (\Phi)^2 \langle \text{Var}(\tilde{V}_i^*(\tau, t) \tilde{V}_j(\tau, t)) \rangle_{i \neq j, \text{LST}} \quad (13)$$

$$= (\Phi)^2 \langle \text{Var}((s + n_i)^*(s + n_j)) \rangle_{i \neq j, \text{LST}} \quad (14)$$

$$= (\Phi)^2 \langle \text{Var}(s^2 + sn_i^* + sn_j + n_i^* n_j) \rangle_{i \neq j, \text{LST}} \quad (15)$$

$$= (\Phi)^2 \langle s^2 \text{Var}(n_i^*) + s^2 \text{Var}(n_j) + \text{Var}(n_i^* n_j) \rangle_{i \neq j, \text{LST}} \quad (16)$$

$$= (\Phi)^2 \langle (2s^2 \text{Var}(n_j) + \text{Var}(n_i^* n_j)) \rangle_{i \neq j, \text{LST}} \quad (17)$$

$$= (\Phi)^2 \langle (2s^2 \text{Var}(n_i) + E[n_i n_i^* n_j n_j^*] - |E[n_i^* n_j]|^2) \rangle_{i \neq j, \text{LST}} \quad (18)$$

$$= (\Phi)^2 \langle 2s^2 \text{Var}(n_i) + E[|n_i|^2] E[|n_j|^2] \rangle_{i \neq j, \text{LST}} \quad (19)$$

$$= (\Phi)^2 \langle 2s^2 \text{Var}(n_i) + \text{Var}(n_i^2) \rangle_{i \neq j, \text{LST}} \quad (20)$$

$$= (\Phi)^2 \left\langle 2 \frac{P_s(k) P_N(k)}{\Phi^2} + \frac{P_N(k)^2}{\Phi^2} \right\rangle_{i \neq j, \text{LST}} \quad (21)$$

$$= \langle 2P_s(k) P_N(k) + P_N(k)^2 \rangle_{i \neq j, \text{LST}}, \quad (22)$$










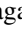

where we assumed each n_i are independent random variables as mentioned above, and all constants of proportionality were used to transform the power spectra from functions of delay, τ ,

³⁴ This assumption does ignore the correlations induced between visibilities that share a common antenna and thus have correlated noise.

to cosmological wavenumber, k . This derivation assumes noise is independent across all baselines. It also assumes the power spectrum and noise are independent in time. In general, these assumptions may not be true and would contribute to additional covariance terms in the expansion of the ensemble average in Equation (12).

At high-delay modes, foreground signals are predicted to have little power (e.g., $P_s(k) \rightarrow 0$), and the variance reduces to the thermal variance P_N . Conversely, inside the horizon and at delay modes just outside the horizon, this variance will be dominated by the term dependent on the power spectrum of the true sky $P_s(k)$.

ORCID iDs

Matthew Kolopanis  <https://orcid.org/0000-0002-2950-2974>
 Daniel C. Jacobs  <https://orcid.org/0000-0002-0917-2269>
 Saul A. Kohn  <https://orcid.org/0000-0001-6744-5328>
 James E. Aguirre  <https://orcid.org/0000-0002-4810-666X>
 Gianni Bernardi  <https://orcid.org/0000-0002-0916-7443>
 Chris L. Carilli  <https://orcid.org/0000-0001-6647-3861>
 Joshua S. Dillon  <https://orcid.org/0000-0003-3336-9958>
 Joshua Kerrigan  <https://orcid.org/0000-0002-1876-272X>
 Adrian Liu  <https://orcid.org/0000-0001-6876-0928>
 Nithyanandan Thyagarajan  <https://orcid.org/0000-0003-1602-7868>
 Chuneeta D. Nunhokee  <https://orcid.org/0000-0002-5445-6586>

References

- Ali, S. S., Bharadwaj, S., & Chengalur, J. N. 2008, *MNRAS*, **385**, 2166
 Ali, Z. S., Parsons, A. R., Zheng, H., et al. 2015, *ApJ*, **809**, 61
 Ali, Z. S., Parsons, A. R., Zheng, H., et al. 2018, *ApJ*, **863**, 201
 Andrae, R. 2010, arXiv:1009.2755
 Astropy Collaboration, Robitaille, T. P., Tollerud, E. J., et al. 2013, *A&A*, **558**, A33
 Barkana, R., & Loeb, A. 2001, *PhR*, **349**, 125
 Barkana, R., & Loeb, A. 2007, *RPPH*, **70**, 627
 Beardsley, A. P., Hazelton, B. J., Sullivan, I. S., et al. 2016, *ApJ*, **833**, 102
 Bernardi, G., de Bruyn, A. G., Brentjens, M. A., et al. 2009, *A&A*, **500**, 965
 Bernardi, G., de Bruyn, A. G., Harker, G., et al. 2010, *A&A*, **522**, A67
 Bernardi, G., Greenhill, L. J., Mitchell, D. A., et al. 2013, *ApJ*, **771**, 105
 Bernardi, G., Zwart, J. T. L., Price, D., et al. 2016, *MNRAS*, **461**, 2847
 Bowman, J. D., & Rogers, A. E. E. 2010, *Natur*, **468**, 796
 Cheng, C., Parsons, A. R., Kolopanis, M., et al. 2018, *ApJ*, **868**, 26
 Clark, B. G. 1999, in ASP Conf. Ser. 180, Synthesis Imaging in Radio Astronomy II, ed. G. B. Taylor, C. L. Carilli, & R. A. Perley (San Francisco, CA: ASP), 1
 Cotton, W. D., Condon, J. J., Perley, R. A., et al. 2004, *Proc. SPIE*, **5489**, 180
 de Oliveira-Costa, A., Tegmark, M., Gaensler, B. M., et al. 2008, *MNRAS*, **388**, 247
 DeBoer, D. R., Parsons, A. R., Aguirre, J. E., et al. 2017, *PASP*, **129**, 045001
 Dillon, J. S., Kohn, S. A., Parsons, A. R., et al. 2018, *MNRAS*, **477**, 5670
 Dillon, J. S., Liu, A., Williams, C. L., et al. 2014, *PhRvD*, **89**, 023002
 Dillon, J. S., Neben, A. R., Hewitt, J. N., et al. 2015, *PhRvD*, **91**, 123011
 Efron, B., & Tibshirani, R. 1994, An Introduction to the Bootstrap (London: Taylor and Francis)
 Furlanetto, S. R., Oh, S. P., & Briggs, F. H. 2006, *PhR*, **433**, 181
 Ghosh, A., Bharadwaj, S., Ali, S. S., & Chengalur, J. N. 2011, *MNRAS*, **418**, 2584
 Górski, K. M., Hivon, E., Banday, A. J., et al. 2005, *ApJ*, **622**, 759
 Greig, B., Mesinger, A., & Pober, J. C. 2016, *MNRAS*, **455**, 4295
 Hazelton, B., Beardsley, A., Pober, J., et al. 2017, HERA-Team/pyuvdata: Version 1.2, Zenodo, doi:10.5281/zenodo.1044022
 Högbom, J. A. 1974, *A&AS*, **15**, 417
 Hurley-Walker, N., Callingham, J. R., Hancock, P. J., et al. 2017, *MNRAS*, **464**, 1146
 Iglewicz, B., & Hoaglin, D. C. 1993, in How to Detect and Handle Outliers, ed. P. Edward & F. Mykytko (AQSC Quality Press), 16
 Intema, H. T., van der Tol, S., Cotton, W. D., et al. 2009, *A&A*, **501**, 1185
 Jacobs, D. C., Hazelton, B. J., Trott, C. M., et al. 2016, *ApJ*, **825**, 114
 Jacobs, D. C., Parsons, A. R., Aguirre, J. E., et al. 2013, *ApJ*, **776**, 108
 Jacobs, D. C., Pober, J. C., Parsons, A. R., et al. 2015, *ApJ*, **801**, 51
 Jones, E., Oliphant, T., Peterson, P., et al. 2001, SciPy: Open Source Scientific Tools for Python, version 1.2.1, <http://www.scipy.org/>
 Joseph, R. C., Trott, C. M., & Wayth, R. B. 2018, *AJ*, **156**, 285
 Kerrigan, J. R., Pober, J. C., Ali, Z. S., et al. 2018, *ApJ*, **864**, 131
 Lanham, A., Hazelton, B., Jacobs, D., et al. 2019, *JOSS*, **4**, 1234
 Liu, A., & Parsons, A. R. 2016, *MNRAS*, **457**, 1864
 Liu, A., Parsons, A. R., & Trott, C. M. 2014a, *PhRvD*, **90**, 023018
 Liu, A., Parsons, A. R., & Trott, C. M. 2014b, *PhRvD*, **90**, 023019
 Liu, A., Tegmark, M., Morrison, S., Lutomirski, A., & Zaldarriaga, M. 2010, *MNRAS*, **408**, 1029
 Loeb, A., & Furlanetto, S. R. 2013, *MNRAS*, **408**, 1029
 McKinley, B., Yang, R., López-Cañiego, M., et al. 2015, *MNRAS*, **446**, 3478
 McMullin, J. P., Waters, B., Schiebel, D., Young, W., & Golap, K. 2007, in ASP Conf. Ser. 376, Astronomical Data Analysis Software and Systems XVI, ed. R. A. Shaw, F. Hill, & D. J. Bell (San Francisco, CA: ASP), 127
 Mellema, G., Koopmans, L. V. E., Abdalla, F. A., et al. 2013, *ExA*, **36**, 235
 Mesinger, A., Furlanetto, S., & Cen, R. 2011, *MNRAS*, **411**, 955
 Moore, D. F., Aguirre, J. E., Kohn, S. A., et al. 2017, *ApJ*, **836**, 154
 Morales, M. F., & Wyithe, J. S. B. 2010, *ARA&A*, **48**, 127
 Mort, B. J., Dulwich, F., Salvini, S., Adami, K. Z., & Jones, M. E. 2010, in 2010 IEEE Int. Symp. on Phased Array Systems and Technology (ARRAY) (Piscataway, NJ: IEEE), 690
 Oh, S. P. 2001, *ApJ*, **553**, 499
 Oliphant, T. 2006, NumPy: A Guide to NumPy (USA: Trelgol Publishing)
 Paciga, G., Albert, J. G., Bandura, K., et al. 2013, *MNRAS*, **433**, 639
 Parsons, A., Pober, J., McQuinn, M., Jacobs, D., & Aguirre, J. 2012a, *ApJ*, **753**, 81
 Parsons, A. R., & Backer, D. C. 2009, *AJ*, **138**, 219
 Parsons, A. R., Backer, D. C., Foster, G. S., et al. 2010, *AJ*, **139**, 1468
 Parsons, A. R., Liu, A., Aguirre, J. E., et al. 2014, *ApJ*, **788**, 106
 Parsons, A. R., Liu, A., Ali, Z. S., & Cheng, C. 2016, *ApJ*, **820**, 51
 Parsons, A. R., Pober, J. C., Aguirre, J. E., et al. 2012b, *ApJ*, **756**, 165
 Patil, A. H., Yatawatta, S., Koopmans, L. V. E., et al. 2017, *ApJ*, **838**, 65
 Patra, N., Subrahmanyan, R., Sethi, S., Udaya Shankar, N., & Raghunathan, A. 2015, *ApJ*, **801**, 138
 Pober, J. C., Ali, Z. S., Parsons, A. R., et al. 2015, *ApJ*, **809**, 62
 Pober, J. C., Hazelton, B. J., Beardsley, A. P., et al. 2016, *ApJ*, **819**, 8
 Pober, J. C., Liu, A., Dillon, J. S., et al. 2014, *ApJ*, **782**, 66
 Pober, J. C., Parsons, A. R., Aguirre, J. E., et al. 2013, *ApJL*, **768**, L36
 Pober, J. C., Parsons, A. R., Jacobs, D. C., et al. 2012, *AJ*, **143**, 53
 Pritchard, J. R., & Loeb, A. 2010, *PhRvD*, **82**, 023006
 Rogers, A. E. E., & Bowman, J. D. 2008, *AJ*, **136**, 641
 Santos, M. G., Cooray, A., & Knox, L. 2005, *ApJ*, **625**, 575
 Sokolowski, M., Tremblay, S. E., Wayth, R. B., et al. 2015, *PASA*, **32**, 4
 Sullivan, I. S., Morales, M. F., Hazelton, B. J., et al. 2012, *ApJ*, **759**, 17
 Thyagarajan, N., Jacobs, D. C., Bowman, J. D., et al. 2015a, *ApJL*, **807**, L28
 Thyagarajan, N., Jacobs, D. C., Bowman, J. D., et al. 2015b, *ApJ*, **804**, 14
 Thyagarajan, N., Kolopanis, M., Jacobs, D., Murray, S., & Santoshmh 2019, PRISim: Precision Radio Interferometry Simulator (for Radio Astronomy Applications), 0.2-alpha, 2, Zenodo, doi:10.5281/zenodo.2548117
 Tingay, S. J., Goeke, R., Bowman, J. D., et al. 2013, *PASA*, **30**, 7
 Voytek, T. C., Natarajan, A., Jáuregui García, J. M., Peterson, J. B., & López-Cruz, O. 2014, *ApJL*, **782**, L9
 Wayth, R. B., Lenc, E., Bell, M. E., et al. 2015, *PASA*, **32**, e025
 Yatawatta, S., de Bruyn, A. G., Brentjens, M. A., et al. 2013, *A&A*, **550**, A136
 Zheng, H., Tegmark, M., Buza, V., et al. 2014, *MNRAS*, **445**, 1084